

---


Electronic Theses and Dissertations, 2004-2019

---

2019

## High Performance Liquid Crystal Devices for Augmented Reality and Virtual Reality

Md Javed Rouf Talukder  
*University of Central Florida*

 Part of the [Electromagnetics and Photonics Commons](#), and the [Optics Commons](#)  
Find similar works at: <https://stars.library.ucf.edu/etd>  
University of Central Florida Libraries <http://library.ucf.edu>

This Doctoral Dissertation (Open Access) is brought to you for free and open access by STARS. It has been accepted for inclusion in Electronic Theses and Dissertations, 2004-2019 by an authorized administrator of STARS. For more information, please contact [STARS@ucf.edu](mailto:STARS@ucf.edu).

---

### STARS Citation

Talukder, Md Javed Rouf, "High Performance Liquid Crystal Devices for Augmented Reality and Virtual Reality" (2019). *Electronic Theses and Dissertations, 2004-2019*. 6583.  
<https://stars.library.ucf.edu/etd/6583>

HIGH PERFORMANCE LIQUID CRYSTAL DEVICES FOR AUGMENTED REALITY  
AND VIRTUAL REALITY

by

MD JAVED ROUF TALUKDER

B.E. University of Electro-Communications, Japan, 2011

M.S. University of Tokyo, Japan, 2013

M.S. CREOL, University of Central Florida, 2016

A dissertation submitted in partial fulfillment of the requirements  
for the degree of Doctor of Philosophy  
in CREOL/The College of Optics & Photonics  
at the University of Central Florida  
Orlando, Florida

Summer Term  
2019

Major Professor: Shin-Tson Wu

© 2019 Md Javed Rouf Talukder

## ABSTRACT

See-through augmented reality and virtual reality displays are emerging due to their widespread applications in education, engineering design, medical, retail, transportation, automotive, aerospace, gaming, and entertainment. For augmented reality and virtual reality displays, high-resolution density, high luminance, fast response time and high ambient contrast ratio are critically needed. High-resolution density helps eliminate the screen-door effect, high luminance and fast response time enable low duty ratio operation, which plays a key role for suppressing image blurs. A dimmer placed in front of AR display helps to control the incident background light, which in turn improves the image contrast. In this dissertation, we have focused three crucial display metrics: high luminance, fast motion picture response time (MPRT) and high ambient contrast ratio.

We report a fringe-field switching liquid crystal display, abbreviated as d-FFS LCD, by using a low viscosity material and new diamond-shape electrode configuration. Our proposed device shows high transmittance, fast motion picture response time, low operation voltage, wide viewing angle, and indistinguishable color shift and gamma shift. We also investigate the rubbing angle ( $\alpha$ ) effects on transmittance and response time. When  $\alpha=0^\circ$ , the virtual wall effect is strong, resulting in fast response time but compromised transmittance. When  $\alpha \geq 1.2^\circ$ , the virtual walls disappear, as a result, the transmittance increases dramatically, but the tradeoff is in slower response time. We also demonstrate a photo-responsive guest-host liquid crystal (LC) dimmer to enhance the ambient contrast ratio in augmented reality displays. The LC composition consists of photo-stable chiral agent,

photosensitive azobenzene, and dichroic dye in a nematic host with negative dielectric anisotropy. In this device, transmittance changes from bright state to dark state by exposing a low intensity UV or blue light. Reversal process can be carried out by red light or thermal effect. Such a polarizer-free photo-activated dimmer can also be used for wide range of applications, such as diffractive photonic devices, portable information system, vehicular head-up displays, and smart window for energy saving purpose. A dual-stimuli polarizer-free dye-doped liquid crystal (LC) device is demonstrated as a dimmer. Upon UV/blue light exposure, the LC directors and dye molecules turn from initially vertical alignment (high transmittance state) to twisted fingerprint structure (low transmittance state). The reversal process is accelerated by combining a longitudinal electric field to unwind the LC directors from twisted fingerprint to homeotropic state, and a red light to transform the cis azobenzene back to trans. Such an electric-field-assisted reversal time can be reduced from ~10s to a few milliseconds, depending on the applied voltage. Considering power consumption, low manufacturing cost, and large fabrication tolerance, this device can be used as a smart dimmer to enhance the ambient contrast ratio for augmented reality displays.

To my three children: Tasnuva, Fabiha and Zayan

## **ACKNOWLEDGMENTS**

First and foremost, I would like to express my gratitude and appreciation to my advisor Professor Shin-Tson Wu for his continuous guidance and support throughout my PhD study. Prof. Wu is the leading expert and scientist in liquid crystal device area. I am blessed and honored being his Ph.D. student. Prof. Wu is always encouraging me to explore new research ideas and is positive toward the outcome. He is also available whenever we need feedback and help from him. I am grateful for everything. Besides, I would like to thank Professor Wu's wife Cho-Yan Hsieh for her warming support toward LCD group.

I would also like to thank my committee members: Prof. M. G. Moharam, Prof. Rodrigo Amezcua Correa, and Prof. Yajie Dong for their time to participate and evaluate my thesis work. Besides, I would like to express my gratitude to Professor David Hagan for his guidance and support toward graduate student.

I am very grateful to all of LCD group members. Specially, I would like to thank Dr. Haiwei Chen, Dr. Yun-Han Lee, Yuge Huang, Guanjun Tan, Hung-Yuan Lin, and Ran Chen for their great support toward my Ph.D. study. Besides, I would like to express my appreciation to Dr. Daming Xu, Dr. Fenglin Peng, Dr. Ruidong Zhu, Fangwang Gou, Juan He, Enguo Chen, Xiaomin Liu, Kun Yin, Tao Zhan, Ziqian He, En-Lin Hsiang, Junyu Zou, and Yannanqi Li.

Besides group member, I am also grateful to my professional colleagues in Qorvo Inc. Specially, I would like to thank Alberto, Meghna, Maria, Hailing, Shogo, Jason, Waleed, Scott, Ahmad, and many other engineers from my company.

I would also like to express my deepest gratitude to my parents, my two brother and one sister for their unconditional love and guidance throughout my personal and educational life.

Finally, I would like to thank my wife Dalia and three children: Jasia, Fabiha and Zayan for their unconditional love and support in my life. Specially, Dalia showed great maturity and patience in rough time in order to pursue a better life. I am indebted to my family for everything what I have done so far.



## TABLE OF CONTENTS

LIST OF FIGURES.....	x
LIST OF TABLES.....	xiv
CHAPTER 1: INTRODUCTION.....	1
1.1. High transmittance and fast response liquid crystal device .....	1
1.2. High ambient contrast ratio smart dimmer.....	3
CHAPTER 2: FRINGE-FIELD SWITCHING MODE.....	6
2.1. Current progress and mechanism of fringe-field switching (FFS) model.....	6
2.2. Key material parameter for high performance .....	14
CHAPTER 3: HIGH TRANSMITTANCE AND FAST-RESPONSE LCD .....	19
3.1. Liquid crystal material.....	19
3.1.1 Birefringence .....	20
3.1.2 Visco-elastic coefficient .....	22
3.2. Device structure .....	23
3.3. Calculated results.....	25
3.3.1 Voltage-dependent transmittance (VT) curves and response time .....	25
3.3.2 Electrode structure optimization.....	29
3.4. Discussion .....	32
3.4.1 Gray-to-gray (GTG) response time .....	34

3.4.2 Viewing angle.....	37
3.4.3 Gamma curve .....	38
3.4.4 Color shift.....	38
3.5. Summary .....	39
CHAPTER 4: PHOTO-RESPONSIVE LIQUID CRYSTAL DIMMER .....	41
4.1. Experiment.....	41
4.2. Mechanism.....	42
4.3. Results and discussion.....	44
4.4. Summary .....	52
CHAPTER 5: DUAL-STIMULI LIQUID CRYSTAL SMART DIMMER .....	53
5.1. Experimental configuration.....	53
5.2. Operation principles .....	54
5.3. Results and discussion.....	57
5.4. Summary .....	71
CHAPTER 6: CONCLUSION .....	72
APPENDIX: STUDENT’S PUBLICATIONS.....	74
REFERENCES .....	77

## LIST OF FIGURES

Figure 1 Device structure of in-plane switching (IPS) mode.....	7
Figure 2 Device structure of fringe-field switching (FFS) mode. ....	8
Figure 3 Electrode structure and liquid crystal’s rubbing direction of conventional FFS mode.....	10
Figure 4 Electrode structure and liquid crystal’s rubbing direction of fast FFS mode.....	11
Figure 5 Electrode structure and rubbing direction (LC) of interdigitated pixel electrodes with alternating tilts. ....	13
Figure 6 (a) Temperature-dependent $\Delta n$ of M1 at $\lambda=633$ nm. (b) $\Delta n$ dispersion of M1 at 25°C. Dots are measured data, and the red lines in (a) and (b) are fitting curves with Eq. (1) and Eq. (2), respectively.....	21
Figure 7 Temperature-dependent visco-elastic coefficient of M1 at $\lambda=633$ nm. Dots are measured data and red line represents the fitting curve with Eq. (3). The fitting parameters are listed in Table 1.....	23
Figure 8 Schematic diagram of the proposed d-FFS structure. (a) Cross-sectional view, and (b) top view. $w$ : electrode width, $g$ : electrode gap, $\varphi$ : electrode tilt angle, and $\alpha$ : LC alignment direction w.r.t. $y$ axis.....	24
Figure 9 Simulated transmittance and response time of d-FFS at different rubbing angle.	26
Figure 10 Simulated VT curves of d-FFS at $\alpha= 0^\circ$ and $1.5^\circ$ , $\lambda=550$ nm.....	27
Figure 11 Simulated response time curves of d-FFS at $\alpha = 0^\circ$ and $1.5^\circ$ .....	28

Figure 12 Simulated VT curves of d-FFS using M1. (a) Keeping electrode gap at 3.0 $\mu\text{m}$ while varying electrode width from 2.0 $\mu\text{m}$ to 4.0 $\mu\text{m}$ . (b) Keeping electrode width at 2.0 $\mu\text{m}$ while varying electrode gap from 2.0 $\mu\text{m}$ to 4.0 $\mu\text{m}$ . .....	29
Figure 13 Calculated response time for p-FFS using UCF-M2 (a) Keeping gap 3.0 $\mu\text{m}$ while varying width from 2.0 $\mu\text{m}$ to 4.0 $\mu\text{m}$ (b) Keeping width 2.0 $\mu\text{m}$ while varying gap from 2.0 $\mu\text{m}$ to 4.0 $\mu\text{m}$ .....	30
Figure 14 Cross-sectional view of the simulated LC director distributions and local relative transmittance of d-FFS cell at (a) $\alpha=0^\circ$ , and (b) $\alpha=1.5^\circ$ rubbing angle.....	33
Figure 15 Simulated isocontrast contour of d-FFS LCD with (a) $\alpha=0^\circ$ (b) $\alpha=1.5^\circ$ using a positive A-plate and a positive C-plate. ....	37
Figure 16 Simulated gamma shift of the film-compensated d-FFS LCD at (a) $\alpha=0^\circ$ and (b) $\alpha=1.5^\circ$ . .....	38
Figure 17 Simulated color shift at (a) $\alpha=0^\circ$ (b) $\alpha=1.5^\circ$ using a quantum dot-enhanced backlight. ....	39
Figure 18 Chemical structure of PSC-01 .....	41
Figure 19 LC director and dye orientations of the proposed photo-sensitive dimmer.....	45
Figure 20 Measured transmission spectra of our LC sample before and after UV exposure. ....	46
Figure 21 See-through image of our smart dimmer: (a) before and (b) after UV exposure.	47
Figure 22 Measured transmission vs. exposure time (UV light). ....	48
Figure 23 Measured transmission vs. exposure time using a blue light $\lambda\approx 450\text{ nm}$ .....	49

Figure 24 Measured transmission vs. exposure time of reversal process using a red HeNe laser beam.....	50
Figure 25 (a) Measured transmittance vs. dyes concentration before and after UV exposure. (b) Contrast ratio vs. dyes concentration.....	51
Figure 26 Microscopic image at (a) initial state, and (b) post UV exposure state.....	52
Figure 27 Operation mechanisms of the proposed device: (a) Initial state, (b) after UV exposure, (c) with a voltage, and (d) removing the voltage and red light.....	55
Figure 28 Measured absorption specturm of 2% dichroic dye in a given LC cell.....	58
Figure 29 Measured absorption anisotropy of Mitsui S428 dye at $\lambda=633$ nm. Red and black dots correspond to the polarization parallel and perpendicular to the LC directors. LC host ZLI-2976.....	59
Figure 30 Measured transmission spectra at initial state, post UV exposure, and after red light exposure.....	60
Figure 31 Measured transmission spectra of post UV exposure state under different voltages.....	61
Figure 32 See-through image behind the dimmer: (a) Initial state, (b) Post UV exposure state, (c) After applying 10V at post UV exposure state (the dark area has no electrode), and (d) After red light irradiation for 15 s at post UV exposure state.....	62
Figure 33 Measured transmittance change at $\lambda=633$ nm of our device upon UV exposure (10 mW/cm <sup>2</sup> ).....	63
Figure 34 Measured transmittance (at 633 nm) vs. response time at post UV exposure state after applying 10 V for 500 ms.....	64

Figure 35 Measured transmittance (at 633 nm) vs. response time at post UV exposure state after applying 50 V for 100 ms. ....	65
Figure 36 Measured time-dependent transmittance of the LC sample from the post exposure state after HeNe laser beam exposure at intensity= 5.5 mW/cm <sup>2</sup> .....	66
Figure 37 Measured time-dependent transmittance of the LC sample from the post exposure state when red light and voltage are applied together at different time interval.....	67
Figure 38 Microscope images of four samples: (a) Initial state (1%-4% S-811), (b) 1% S-811, (c) 3% S-811, and (d) 4% S-811 at post UV exposure state.....	68
Figure 39 Microscopic images of samples(4% S-811): (a) 0.3%-PSC01 (b) 0.7% PSC01 (c) 1.2% PSC01 (d) 1.6% PSC01 at post exposure state.....	69
Figure 40 Measured transmittance at different azobenzene concentrations. $\lambda = 550$ nm... .	70
Figure 41 Measured transmission spectra at initial state (black line) and post UV exposure state (red line) using a low birefringence LC host, ZLI 1800-100. ....	71

## LIST OF TABLES

Table 1 Measured physical properties of M1 at T=25°C and f=1 kHz. ....	20
Table 2 Calculated peak transmittance and response time at the on voltage for 3 LC devices .....	31
Table 3 Calculated GTG response time (ms) of our proposed d-FFS with $\alpha=0^\circ$ .....	34
Table 4 Calculated GTG response time (ms) of our proposed d-FFS with $\alpha=1.5^\circ$ .....	35
Table 5 Calculated GTG response time (ms) of our proposed d-FFS with $\alpha=1.5^\circ$ .....	36
Table 6 Prepared 4 samples using different dichroic dye (S428) concentration .....	50

## CHAPTER 1: INTRODUCTION

### 1.1. High transmittance and fast response liquid crystal device

See-through augmented reality (AR) and virtual reality (VR) displays, such as Google Glass, HoloLens, magic leap one, and Oculus rift, are emerging due to their useful applications in education, engineering design, medical, retail, transportation, automotive, aerospace, gaming, and entertainment, just to name a few [1]-[7]. Presently, thin-film-transistor (TFT) liquid crystal displays (LCDs) and organic light-emitting diode (OLED) displays are two dominating technologies for TVs, smartphones, and AR and VR displays [8]-[11]. Although each technology has its own pros and cons [12], the common trend is ever-increasing resolution density and faster response time. This is particularly important for AR and VR displays in order to mitigate the annoying screen-door effect and image blurs. However, as resolution density increases, display luminance decreases because of the reduced aperture ratio. Lower optical efficiency leads to increased power consumption, i.e. shorter battery lifetime for mobile displays. Another equally important performance metric is image blur, which is governed by the motion picture response time (MPRT) [13]. MPRT is jointly determined by the TFT frame rate, LCD/OLED response time, and duty ratio [14]. Both active matrix LCD and OLED are holding type displays, thus, they would exhibit different degrees of image blurs. Under the same frame rate, say 120 Hz, if an LCD's response time is below 2 ms, then its MPRT is comparable to that of OLED, even its response time is as fast as 1  $\mu$ s. A common approach to suppress the image blur of LCD and OLED is to lower the duty ratio [14] so that they behave CRT-like impulse driving. However, to keep the same luminance,



say 150 nits for VR, we have to boost LCD's backlight brightness or OLED's driving current. As a result, efficiency droop in LED backlight [15] takes place or OLED's lifetime is compromised [16]. Therefore, a high transmittance and fast MPRT LCD is urgently needed for the emerging AR and VR display applications.

Fringe-field switching (FFS) LCD [17] is a favorable choice for high-resolution density panels because of its built-in storage capacitor and weak color shift. The former enables high-resolution density. However, FFS still has some room for improvement, such as limited contrast ratio (CR~2000:1) and relatively slow response time (10-15 ms due to the small twisted elastic constant  $K_{22}$  involved). To improve contrast ratio, mini-LED backlight with area local dimming has been implemented and remarkable result (CR > 100,000:1) has been achieved [18], [19]. To shorten response time, interdigitated pixel-electrode structures with two-dimensional standing layers (also called virtual walls) have been proposed [20]-[23]. These virtual walls exert an additional restoring torque to accelerate the decay process so that the average gray-to-gray (GTG) response time can be reduced to 3-5 ms. However, a significant tradeoff is compromised transmittance due to the existence of virtual walls.

In chapter three, we report a new FFS LCD with diamond-shape electrode structure along with a low viscosity LC mixture to simultaneously achieve high transmittance and fast GTG response time, while preserving the inherent advantages on wide viewing angle and indistinguishable gamma shift and color shift.

## 1.2. High ambient contrast ratio smart dimmer

In an AR system, the computer-generated images are projected to superimpose with the environment [24], [25]. As the ambient brightness increases, the image contrast ratio decreases gradually [26]. To enhance ambient contrast ratio, we could either boost the display luminance or dim the incident background light through a built-in sensor. The former is called adaptive brightness control, while the latter is called smart dimmer. A smart dimmer placed in front of the AR display helps to control the incident background light, which in turn improves the ambient contrast ratio. Recently, several types of smart dimmers have been developed, such as organic and inorganic electrochromic devices [27]-[32], nanoparticle devices [33], [34], and guest-host liquid crystal (LC) devices [24], [26], [35]-[42]. Each approach has its own pros and cons. Guest-host liquid crystal devices [43]-[46], developed in late 1960s, have found renewed interest as smart dimmer for enhancing the ambient contrast ratio of augmented reality displays [24] and smart windows for energy-saving buildings [47], [48]. A guest-host LC usually contains 2-3% absorptive dichroic dyes in a nematic host. Its unique features are electrically controllable transmittance, no need for polarizer, wide viewing angle, low manufacturing cost, and possible usage of flexible plastic substrates [36]. When the long axis of dichroic dyes are parallel to the incident light polarization, the absorption is strong so that the transmittance is low. As the LC directors and dye molecules are reoriented to be perpendicular to the substrates, the absorption is weak and the transmittance is high. The contrast ratio of a guest-host LC device depends on the order parameter, dyes dichroic ratio and concentration, and cell gap.

Two types of polarization-independent guest-host systems have been developed, depending on the driving methods: one is by voltage, and another is by light. Most of above-mentioned guest-host devices belong to the former. In chapter 4, unlike conventional voltage-driven guest-host displays, we demonstrate a photo-sensitive dye-doped cholesteric liquid crystal (CLC) smart dimmer for enhancing the ambient contrast ratio of augmented reality displays. CLCs are self-organized molecules, which form planar helical structures [49], [50]. To prepare a CLC, we can mix some chiral compounds into a nematic host to induce helical structures [41]. Right or left handedness can be chosen based on the nature of chiral dopant and interaction with the host LC. Helical twisting power, which defines the handedness of CLC material, can be controlled by electromagnetic fields, temperature, and concentration of the doping materials [42]. Another way to change the helical twisting power is to irradiate the sample with UV-blue light. When a photosensitive chiral azobenzene compound is doped into a CLC host, it undergoes trans-cis photoisomerization upon UV-blue light exposure [51]-[53]. The helical twisting power of photosensitive molecule varies between rod-shaped trans-state and kink-shaped cis-state. In our proposed guest-host LC system, we utilize this light sensitive nature of azobenzene compounds to control the transmittance of our device. At initial state, the LC directors and dye molecules are aligned perpendicular between two glass plates. Under such condition, the absorption is minimum, i.e. the transmittance is maximum. Upon UV-blue light exposure, the LCs and dye molecules turn into planar state due to photoisomerization where the helical axis is perpendicular to the glass substrates. As the dye's absorption axis is parallel to the incident light polarization,

it absorbs the incident light and the device becomes opaque. Our photo-switchable guest-host LC device can also be used as smart window and windshield for vehicular displays.

In chapter 5, we report a dual-stimuli dye-doped LC smart dimmer with a much faster response time. To achieve dual-stimuli responses, we dope some photo-stable chiral agent, photosensitive azobenzene, and dichroic dye into a nematic LC host with positive dielectric anisotropy ( $\Delta\epsilon > 0$ ). Upon UV light exposure, our device turns from initially vertical alignment (high transmittance state) to twisted fingerprint structure (dark state). The reversal process is accelerated by combining electric field (to unwind the fingerprint to homeotropic alignment) and red light (to transform azobenzene from cis to trans) because the LC host has a positive  $\Delta\epsilon$ . Such an electric-field-assisted reversal time can be reduced from  $\sim 10$  seconds to a few milliseconds, depending on the applied voltage. This device can be used as a smart dimmer in augmented reality system.

## **CHAPTER 2: FRINGE-FIELD SWITCHING MODE**

After about five decades of extensive material research, device development, and heavy investment in manufacturing facilities, liquid crystal displays are ubiquitous. Their applications span from smartphones, pads, notebook computers, monitors, large-size TVs, to projection displays. There are three major liquid crystal operation modes: twisted nematic (TN) for notebooks, vertical alignment (VA) for TVs, and in-plane switching (IPS) for touch panels. Analogous to IPS, fringe-field switching (FFS), which exhibits a higher transmittance and built-in capacitor in each pixel, is a favored choice for touch panels because of its wide viewing angle, high-resolution density, high pressure resistance, weak color shift, and low power consumption.

### **2.1. Current progress and mechanism of fringe-field switching (FFS) model**

In the 1990s, thin-film-transistor (TFT) liquid crystal display (LCD) has become the emerging technology in desktop monitors and notebook screens. TFT LCD was then based on twisted nematic (TN) liquid crystal mode which has low power consumption, and good image quality. In TN mode, LC director is twisted by 90 degrees from top to bottom substrate. Due to LC director's upward tilt, this mode has a relatively narrow viewing angle, which limits its practical uses for large size displays. Therefore, there was an urgent need to get wide a viewing angle in the information display devices. Then, Hitachi reported a wide-view in-plane switching (IPS) TFT LCD to overcome this problem [54]. Figure 1 shows the device structure of in-plane switching (IPS) mode. In this device, LC directors are sandwiched with glass substrates and alignment layer. The bottom polarizer is parallel to the LC directors and

the top analyzer is crossed. Inter-digital electrodes are arranged in the same substrate and it generates fringe-field toward the transverse direction which rotates the LC directors in a plane. Initially, LC molecules are homogeneously aligned at a certain rubbing angle with respect to the electrodes.

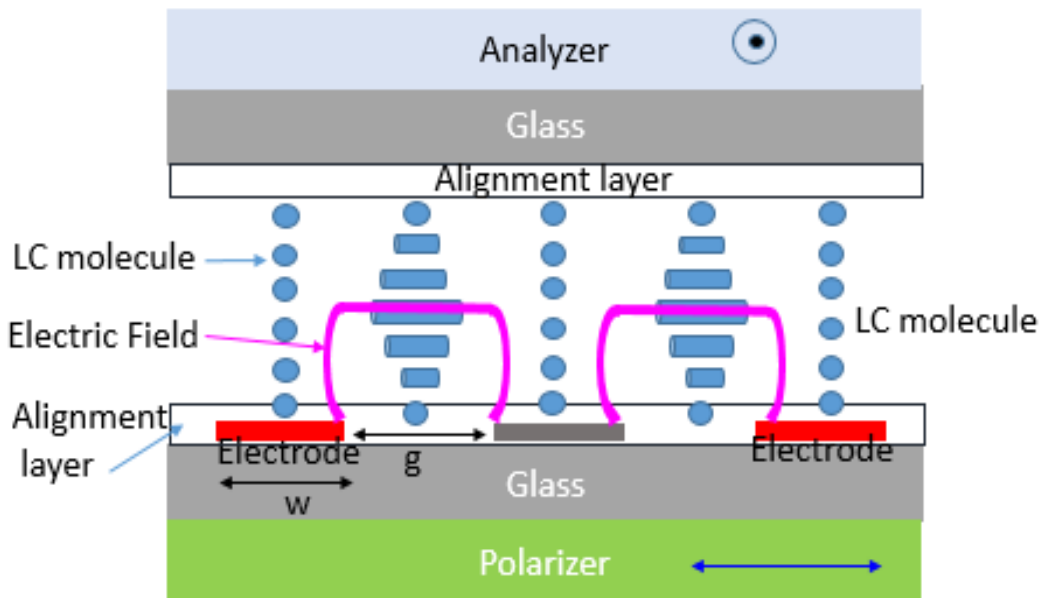


Figure 1 Device structure of in-plane switching (IPS) mode.

At voltage-off state, light cannot pass through the device as incoming light experiences no phase retardation and is absorbed by the crossed analyzer. As the applied voltage increases, the fringing field reorients the LC directors and the incoming light experiences phase retardation. Thus, the device becomes transparent at a voltage-on state. In order to get effective birefringence in IPS device, the LC directors should be reoriented by the in-plane field. Therefore, the electrode width and cell gap should be smaller than the electrode gap. Due to this requirement, transmittance loss above the electrodes is fairly large

because the LC directors at this position cannot rotate enough. In addition, operating voltage is also proportional to the distance between electrodes ( $g$ ).

Although a larger gap will provide a higher transmittance, the tradeoff is higher voltage.

Therefore, it is challenging to get high transmittance and low operating voltage in IPS mode.

In order to resolve this issue, fringe-field switching (FFS) mode has been proposed [55].

Figure 2 shows the device structure of fringe-field switching (FFS) mode. Basic structure of FFS mode is similar to IPS except for the electrode configuration and gap.

As the gap between the electrodes is smaller in FFS device, a strong in-plane field between pixel electrodes and a common electrode exists and it can rotate the LC director

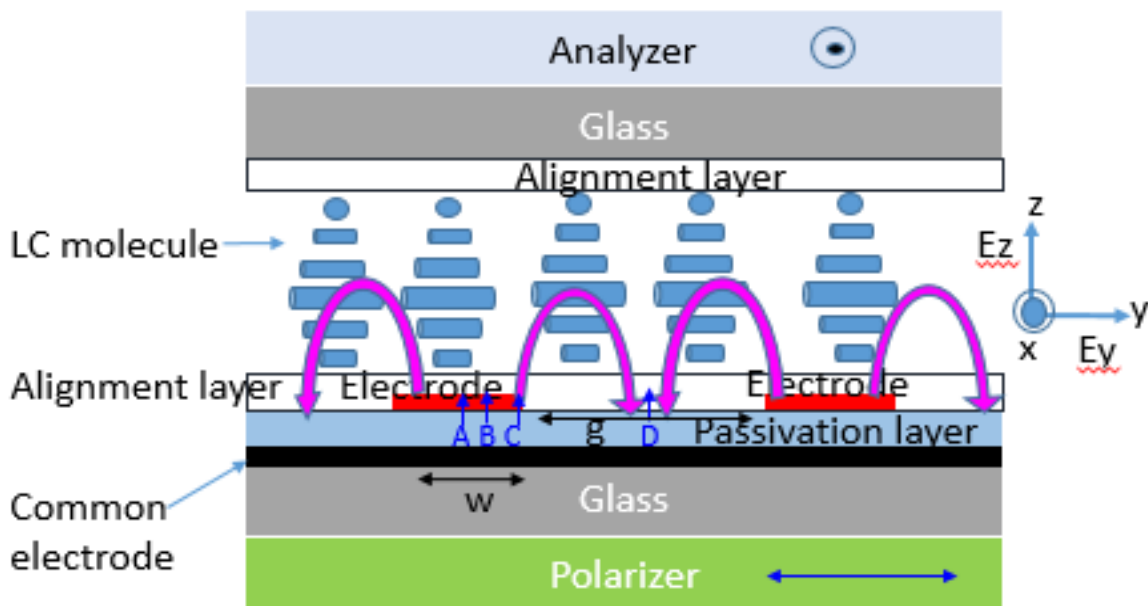


Figure 2 Device structure of fringe-field switching (FFS) mode.

above the surface electrode enough so that it can rotate the LC directors above the center of the electrode. Basically, LC directors above and on the edge of the electrode are rotated by

dielectric torque and elastic torque. Moreover, maximum field intensity of FFS mode just above the electrode is several times higher than the IPS mode as distance between the signal and the ground electrode is smaller. Due to this strong dielectric torque and elastic torque, it rotates whole LC directors above the electrode surfaces and it provides higher transmittance than IPS mode. Moreover, operating voltage in FFS mode is lower than IPS mode as the gap between electrodes is smaller. Thus, it realizes the high transmittance and low operating voltage simultaneously while providing the wide viewing angle because homogeneously aligned directors switch in-plane. Therefore, fringe-field switching mode is the perfect candidate for high performance displays. Besides, fringe-field switching displays have the characteristics of a self-forming storage capacitor. Storage capacitor ( $C_{st}$ ) can be realized between the signal electrode and the ground electrode in light transmitted areas. Unlike other LCD modes, FFS LCD does not require the sacrifice of the aperture ratio for storage capacitor. So, FFS mode is also suitable for high resolution displays. In conventional displays such as twisted nematic (TN) display, when pressure is applied to the panel, strong ripples and strong pooling mura can be easily observed. A thick cover glass with an air gap is required in conventional display to overcome this issue. However, it increases the weight and system cost while decreasing the transmittance. Unlike conventional LCD, FFS LCD does not show ripples and pooling mura when it is touched down by pen or fingers. This feature makes FFS mode unique in touch screen display. Therefore, FFS display has been widely used in mobile displays because of its several outstanding features.

However, conventional fringe-field switching (FFS) mode suffers slow response time. Unlike other LC modes such as VA where  $K_{33}$  dominates the response time, in FFS mode,



twist elastic coefficient ( $K_{22}$ ) and splay elastic coefficient ( $K_{11}$ ) play a role for LC response time. As twist elastic coefficient,  $K_{22}$  is near to half of bend elastic coefficient,  $K_{33}$ , response time becomes longer in FFS mode. Slow response time causes image degradation and motion blur in vehicle displays and virtual reality displays. Moreover, there is an industrial requirement for all vehicle displays to operate in all possible ambient temperatures. When ambient temperature goes down, response time of LC becomes slower. Therefore, fast response time is another critical requirement for vehicle displays and virtual reality displays to suppress the motion blur of moving objects.

Several approaches have been proposed to get fast response time in fringe-field switching mode. Although each approach has its pros and cons, fast fringe-field switching of a liquid crystal device with virtual walls have been proposed recently to overcome slow response time in FFS mode [22]. In conventional LCD, LC molecules have a 7-10 degree rubbing angle with a small tilt when positive dielectric anisotropy material is used.

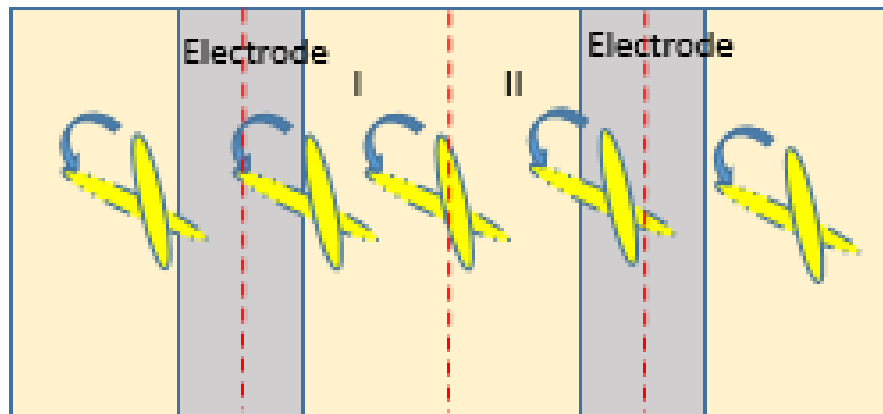


Figure 3 Electrode structure and liquid crystal's rubbing direction of conventional FFS mode.

Figure 3 shows the top view of conventional fringe-field switching structures. Unlike conventional LCD, in fast fringe-field switching LCD, response time can be decreased by introducing a zero-degree rubbing angle where LC molecules are confined in two dimensions by virtual walls. Figure 4 shows the virtual wall formed in the center of the gap between two electrodes in fast fringe-field switching mode.

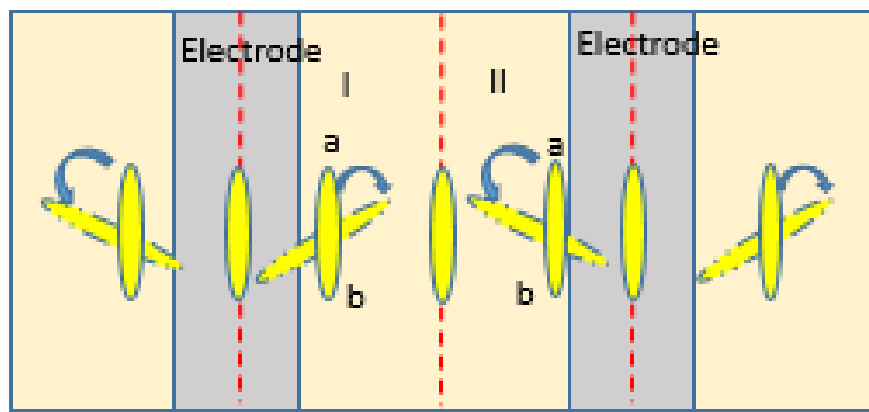


Figure 4 Electrode structure and liquid crystal's rubbing direction of fast FFS mode

Initially, LC molecules are aligned homogeneously with zero degree rubbing angle and non-zero pretilt angle. In this proposed method, if the pretilt angle is zero, LC molecules rotate indeterminate as the direction of the fringe field is perpendicular to the LC molecules. When pretilt angle is non-zero, fringe-field breaks the symmetry of the rotational torque and the tilted ends of the LC molecules are rotated along the electric field direction due to the imbalance of anchoring energy. Direction of the in-plane component of electric fields in region I and region II are different and LC molecules in these two regions are rotated in opposite direction. LC directors in boundaries do not rotate due to the nonexistence of the in-plane component of electric field. In FFS cell with nonzero rubbing angle, LC molecules

near to the edge of the electrode rotate rapidly where the in-plane component of the applied electric field is high. In the boundary of region I and II, as Figure 3 depicts, LC molecules are reoriented by elastic torque, which results in a slow rise time. However, in fast FFS with a zero-degree rubbing angle, rise time is dictated by dielectric torque as LC directors in boundaries of region I and region II in Figure 4 are not rotated by elastic torque. Thus, the rise time of this proposed device is faster than that of a traditional FFS device. Moreover, elastic energy of this device is high as directors in the boundaries are not rotated by elastic torque. Therefore, fast decay time is obtained. In addition to fast response time, fast fringe-field switching (FFS) device with virtual walls shows smaller off-axis color shift than a conventional device due to the multi-domain effect induced by virtual walls.

However, the main tradeoff of fast field switching mode is its compromised transmittance. In the fast FFS mode, transmittance drops significantly in the middle section of the electrode and in the center of the gap. In fast FFS mode, LC directors in these regions do not move due to the formation of virtual walls. Therefore, the incoming light passing through these regions does not experience birefringence. Thus, overall transmittance is reduced in fast FFS mode. Another tradeoff of this device is the requirement of non-zero pretilt angle which limits the viewing angle. Moreover, this device is sensitive to the rubbing angle, and it has narrow process margin.

Interdigitated pixel-electrode structures with alternating tilts for fast fringe-field switching of liquid crystal device has been proposed to overcome the narrow viewing angle and process margin [56]. Figure 5 shows the pixel electrode structure of alternating tilts device.

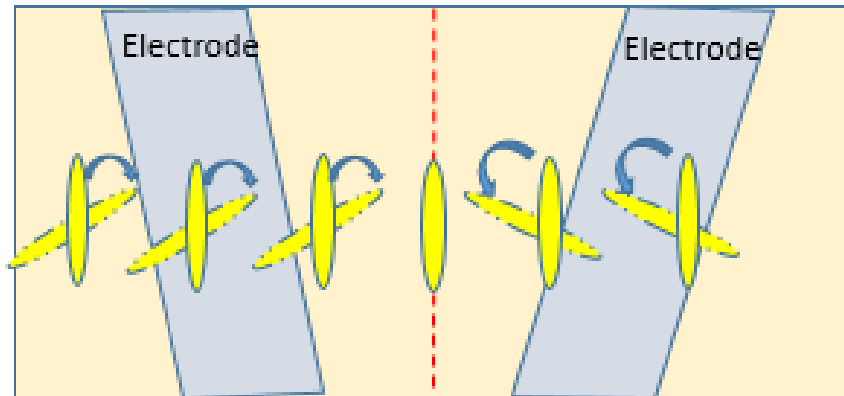


Figure 5 Electrode structure and rubbing direction (LC) of interdigitated pixel electrodes with alternating tilts.

Unlike fast fringe- field switching device where electrodes structure are parallel to the LC alignment direction, electrodes in this device are tilted. As symmetry is broken on top of the electrode, virtual wall only exists in the center of the electrode gap. LC molecules on top of electrodes are rotated by elastic torque from neighboring molecules and LC molecules in the center of the electrode gap do not rotate due to the nonexistence of in-plane field. Although this device provides relatively slow response time, it does not require non-zero pretilt angle which can provide a much wider viewing angle. Moreover, photo-alignment technology, which has been introduced to get high alignment uniformity, high contrast ratio, and wide viewing angle, can also be implemented in this device due to the zero pretilt angle. Moreover, this proposed device allows a much larger deviation of the LC alignment direction. However,

this device still suffers low transmittance due to the virtual walls. Therefore, there is an urgent requirement to get high transmittance for high resolution displays.

## 2.2. Key material parameter for high performance

Along with device structure and rubbing angle, liquid crystal material plays a critical role for high performance in fringe-field switching (FFS) device. Response time is one of the most critical parameters for FFS display. Specially, fast response prevents image quality degradation and motion blur in liquid crystal devices. Recently, field sequential color technology, which can replace color filter, is considered very attractive for high-resolution display. Sub-millisecond response time is required to implement this field sequential color technology display. However, response time of FFS device depends on physical properties of liquid crystal material. The rise and decay time of conventional LC device is given as:

$$\tau_{rise} = \frac{\gamma_1 d^2 / K_{22} \pi^2}{(V / V_{th})^2 - 1} \quad (2.1)$$

$$\tau_{decay} = \frac{\gamma_1 d^2}{K_{22} \pi^2} \quad (2.2)$$

In these equations,  $\gamma_1$ ,  $K_{22}$ , and  $d$  are rotational viscosity, twist elastic coefficient, and cell gap.  $V$  and  $V_{th}$  are operating voltage and threshold voltage. Rise time is directly proportional to rotational viscosity and cell gap. Therefore, it is required to get lower viscosity and thinner cell to get fast rise time. Moreover, rise time of FFS LCD is inversely proportional to the operating voltage. The higher the operating voltage and the lower the threshold voltage, the

faster the rise time. However, decay time does not depend on the operating voltage, and it is typically slower than rise time as this is limited by the slow relaxation time. In addition, rise and decay time depends on twist elastic coefficient,  $K_{22}$ . However, twist elastic coefficient,  $K_{22}$  is smaller than splay elastic coefficient,  $K_{11}$  and bend elastic coefficient,  $K_{33}$ . Therefore, FFS mode suffers slower response time than vertical mode (VA) due to this inherent physical properties of LCs. In addition, rotational viscosity,  $\gamma_1$ , is related to temperature as  $\gamma_1 \sim \exp(E/k_B T)$  where  $E$ ,  $k_B$  and  $T$  are the activation energy, Boltzmann constant and absolute temperature, respectively. So, rotational viscosity increases exponentially when temperature decreases. Low activation energy and low rotational viscosity LC materials are attractive as it provides fast response time in low temperature. Along with response time, operating voltage is also another critical parameter for device performance in order to reduce the power consumption. Operating voltage depends on the threshold voltage, and threshold voltage in FFS device is approximated as following [57]:

$$V_{th} = \pi \sqrt{\frac{K_{22}}{\epsilon_0 \Delta \epsilon}} \quad (2.3)$$

Where  $K_{22}$ ,  $\epsilon_0$  and  $\Delta \epsilon$  are twist elastic coefficient, permittivity of vacuum, and dielectric anisotropy. In order to reduce the operating voltage, it is required to get higher dielectric anisotropy material. However, there is a tradeoff in large dielectric anisotropy material. Higher dielectric material increases the viscosity which in turn increases the response time. Besides, it also increases ionic impurity, which causes image sticking [58]. Therefore, it is

required to get balanced dielectric anisotropy material considering response time and operating voltage.

In IPS mode, transmittance is not dependent on dielectric anisotropy of LC as in-plane fields rotate the liquid crystals. However, in fringe-field switching (FFS) mode, transmittance depends on the sign of the dielectric anisotropy as the tilt angle of the LC above the electrode depends on it. Negative FFS (n-FFS) mode shows higher transmittance (~10% more) than positive FFS mode though it has slower response time than p-FFS mode. Both positive and negative dielectric anisotropy ( $\Delta\epsilon = \epsilon_{//} - \epsilon_{\perp}$ ) materials can be used in fringe-field switching mode. However, positive dielectric anisotropy material (p-FFS) dominates in mobile displays due to its low operational voltage, no image sticking and no grayscale inversion. In order to use p-FFS mode in high resolution displays, there is an urgent need to get high transmittance while maintaining fast response.

J.W. Ryu et.al proposed that transmittance of p-FFS mode depends on the magnitude of dielectric anisotropy ( $\Delta\epsilon$ ) [59]. When voltage is applied to the device, then fringe-field with horizontal ( $E_y$ ) and vertical field ( $E_z$ ) are generated which rotate the LC above the electrode surface. In Figure 2, the LC directors on top of position C are twisted by dielectric torque proportional to  $E_y$ , which provides higher transmittance than position A and position B. As there is no horizontal field ( $E_y$ ) in position A, LC molecules above this position are rotated by elastic torque of the neighboring liquid crystal directors (position B) [59]. Specially, in p-FFS mode when LC directors in position B tilt too much, it provides less elastic torque to directors in position A and thus reduces the transmittance. Magnitude of dielectric anisotropy in p-FFS determines the tilt amount of LC directors in position B which ultimately determine the

twist angle of LC molecules in position A. Transmittance in p-FFS depends on the electrode position. Here, transmittance above the electrode are compared using two liquid crystal materials, LC1 and LC2. Dielectric anisotropy of LC1 ( $\Delta\epsilon=5$ ) is lower than that of LC2 ( $\Delta\epsilon=9$ ). Twist angle of LC in position A determines the transmittance, and twist angle of this position is determined by the tilt angle of LC in position B (Figure 2). When tilt angle of LC1 and LC2 molecules is calculated in position B, it was shown that tilt angle of LC2 is higher than tilt of LC1. This is due to the stronger vertical field component ( $E_z$ ) in LC2 which has higher dielectric anisotropy. As a result, different tilt angle of LC in position B causes different twist angle at position A. At position A, twist angle of LC1 is higher than twist angle of LC2 (Figure 2). Transmittance is proportional to the twist angle of LC molecules. Therefore, transmittance of LC2 devices decreases more than transmittance of LC1 [59]. Thus, unlike twisted nematic (TN) and in-plane switching (IPS) mode, magnitude of dielectric anisotropy plays a critical role for transmittance. This concept can be utilized to the development of high-resolution displays where transmittance is important.

Recently, S.-W. Kang et al proposed that by controlling perpendicular component of dielectric constant of liquid crystal, transmittance of positive fringe-field switching liquid crystal device can be increased [60]. As shown in Figure 2, transmittance at position A, B, and D depends on the perpendicular component of dielectric constant whether transmittance at position C is the same. As perpendicular dielectric component increases from 2 to 8, transmittance increases accordingly in position A, B and D (Figure 2). When large value of perpendicular dielectric component is employed, it reduces the tilt angle of LC molecules at position B [60]. Thus, elastic torque for LC molecules at position A increases



which twist the LC more efficiently, and hence the high transmittance is obtained in p-FFS device. It has been shown that at fixed dielectric anisotropy ( $\Delta\epsilon=8$ ), higher perpendicular dielectric component improves the transmittance in the p-FFS device [60]. This proposed idea helps to select the LC material to increase the transmittance while maintaining same operational voltage.

## CHAPTER 3: HIGH TRANSMITTANCE AND FAST-RESPONSE LCD

In this chapter, new fringe-field switching (FFS) liquid crystal device will be introduced for augmented reality and virtual reality applications. The goal of this device is to improve the transmittance and response time. Formulation of this new liquid crystal material and working principle of proposed electrode structure will be explained in this section. Experimental measurement of birefringence and visco-elastic coefficient of formulated liquid crystal material will be discussed. Simulated results of voltage-transmittance (VT) curves and response time of our proposed structure with this new liquid crystal material will be shown. We also demonstrate the comparison of our optimized device with traditional structure. In addition, we will discuss the gray-to-gray (GTG) response time, motion picture response time (MPRT), viewing angle, gamma curve, and color shift of our proposed device.

### 3.1. Liquid crystal material

To obtain high transmittance in a thin cell gap (e.g. 2.5-3.0  $\mu\text{m}$ ), we should use a slightly higher birefringence ( $\Delta n \sim 0.12$ ) LC material. Meanwhile, a modest dielectric anisotropy ( $\Delta\epsilon = \epsilon_{//} - \epsilon_{\perp}$ ) is required for keeping operation voltage below 6V. However, the polar groups contributing to enhance  $\Delta\epsilon$  will also lead to an increased viscosity. To achieve high transmittance and fast response time, while keeping low operation voltage, we formulated a high  $\Delta n$  LC mixture with balanced dielectric anisotropy and viscosity. Actually, DIC-LC2 (DIC Corp.) exhibits a very low rotational viscosity and relatively high birefringence, except that

its dielectric anisotropy is somewhat too small ( $\Delta\epsilon \approx 1.7$  at 21°C) [61]. Therefore, to increase  $\Delta\epsilon$ , we mixed 80.9% DIC-LC2 with 19.1% DIC-LC3 ( $\Delta\epsilon \approx 8.8$ ). For convenience, we call this experimental mixture as M1. The measured rotational viscosity ( $\gamma_1$ ), birefringence, dielectric anisotropy, splay elastic constant ( $K_{11}$ ), twist elastic constant ( $K_{22}$ ), and activation energy ( $E_a$ ) are listed in Table 1. Melting temperature ( $T_m$ ) and clearing temperature ( $T_c$ ) were measured by Differential Scanning Calorimetry (DSC, TA instruments Q100).

Table 1 Measured physical properties of M1 at T=25°C and f=1 kHz.

LC mixture	$\Delta n @ \lambda=550\text{nm}$	$\epsilon_{//}$	$\epsilon_{\perp}$	$\Delta\epsilon$	$\gamma_1$ (mPa·s)	$K_{11}$ (pN)	$K_{22}$ (pN)	$T_m$ (°C)	$T_c$ (°C)	$E_a$ (meV)
M1	0.1225	5.53	2.87	2.66	35.75	9.93	6.03	-34.5	76.7	248.1

### 3.1.1 Birefringence

To measure the birefringence of M1, we used a commercial homogeneous cell with cell gap 7.65  $\mu\text{m}$ . After injecting M1 into a homogeneous cell, we placed the cell on a Linkam heating stage which was controlled by TMS94 temperature programmer. We then sandwiched this cell between crossed polarizers and applied 1-kHz square-wave AC voltage to this LC cell. A He-Ne laser ( $\lambda=633 \text{ nm}$ ) was used as probing beam. Birefringence was calculated from the measured phase retardation. Figure 6(a) depicts the temperature dependent birefringence at  $\lambda=633 \text{ nm}$ , where dots are measured data and solid red line is fitting with Haller's semi-empirical equation [62]:

$$\Delta n = \Delta n_0 S = \Delta n_0 (1 - T / T_c)^\beta. \quad (3.1)$$

In Eq. (3.1),  $T$  is the Kelvin temperature,  $T_c$  is the clearing point of LC,  $\Delta n_0$  is the extrapolated birefringence at  $T=0$ ,  $S$  is the order parameter, and  $\beta$  is a material constant. From fittings, we obtained  $\Delta n_0=0.1681$  and  $\beta = 0.1851$  for M1.

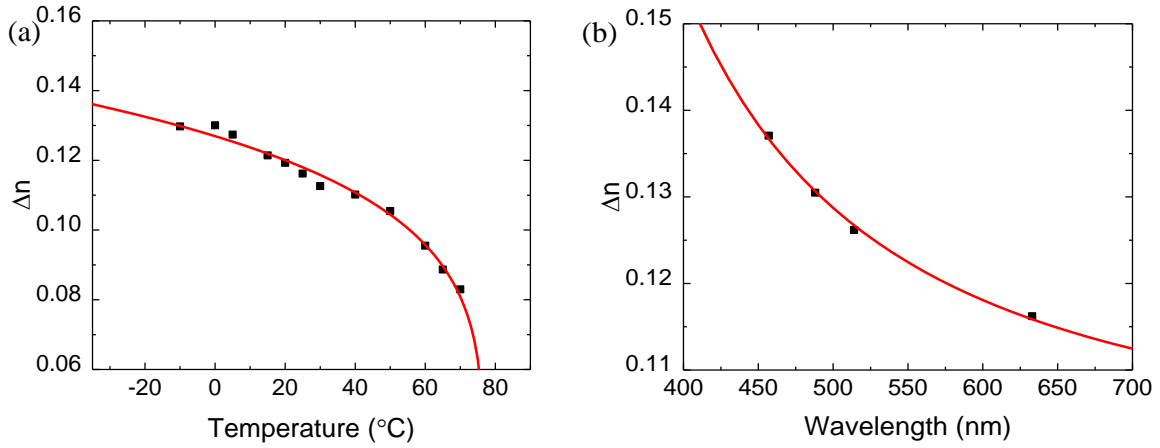


Figure 6 (a) Temperature-dependent  $\Delta n$  of M1 at  $\lambda=633$  nm. (b)  $\Delta n$  dispersion of M1 at  $25^{\circ}\text{C}$ . Dots are measured data, and the red lines in (a) and (b) are fitting curves with Eq. (1) and Eq. (2), respectively.

Next, we measured the wavelength dispersion of M1 by using a He-Ne laser ( $\lambda=633$  nm) and a tunable argon ion laser ( $\lambda=457$  nm,  $488$  nm, and  $514$  nm). Results are plotted in Figure 6(b), where dots are measured results and solid line is the fitting curve with single-band birefringence dispersion equation [63]:

$$\Delta n = G \frac{\lambda^2 \lambda^{*2}}{\lambda^2 - \lambda^{*2}}. \quad (3.2)$$

In Eq. (3.2),  $G$  is the proportionality constant and  $\lambda^*$  is the mean resonance wavelength. Through fittings, we obtained  $G=1.740 \mu\text{m}^{-2}$  and  $\lambda^*= 0.239 \mu\text{m}$ . Using these parameters and Eq. (3.2), we find  $\Delta n= 0.138, 0.123, 0.115$  at  $\lambda=450 \text{ nm}, 550 \text{ nm}, 650 \text{ nm}$ , respectively. Later, we will use these data in our device simulation.

### 3.1.2 Visco-elastic coefficient

To determine the visco-elastic coefficient, we measured the transient decay time of M1 in a homogeneous cell. Results are shown in Figure 7, where dots are experimental data and solid line represents the fitting with following equation [64]:

$$\frac{\gamma_1}{K_{11}} = A \frac{\exp(E_a / k_B T)}{(1 - T / T_c)^\beta}. \quad (3.3)$$

In Eq. (3.3),  $A$  is the proportionality constant,  $k_B$  is the Boltzmann constant, and  $E_a$  is the activation energy. From fittings, we obtained  $E_a = 248.1 \text{ meV}$ . From Figure 7, we find  $\gamma_1/K_{11} = 3.60 \text{ ms}/\mu\text{m}^2$  at  $T=25^\circ\text{C}$ . Through threshold voltage measurement (not shown here), we found  $K_{11} = 9.93 \text{ pN}$ , and subsequently  $\gamma_1 = 35.75 \text{ mPas}$  at  $25^\circ\text{C}$ .

In order to obtain  $K_{22}$ , we filled M1 into a commercial IPS (in-plane switching) cell with  $3\text{-}\mu\text{m}$  cell gap and measured its transient decay time [65]. From the decay time constant, we extracted  $\gamma_1/K_{22} = 5.93 \text{ ms}/\mu\text{m}^2$  at  $25^\circ\text{C}$ . From the already obtained  $\gamma_1$ , we can calculate the twist elastic coefficient and result is  $K_{22} = 6.03 \text{ pN}$ . We will use these parameters in our device simulations discussed below.

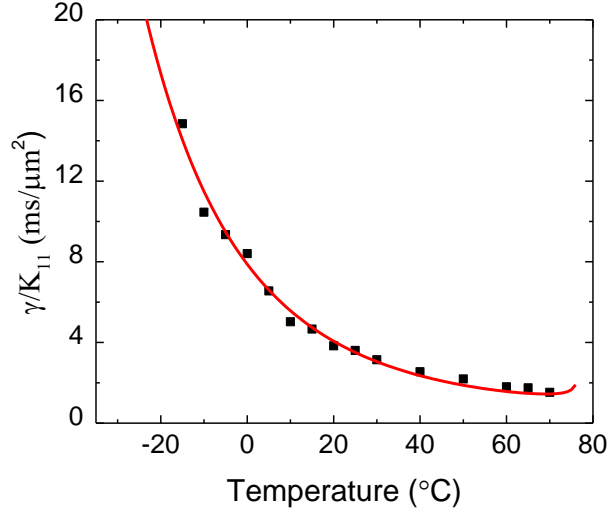


Figure 7 Temperature-dependent visco-elastic coefficient of M1 at  $\lambda=633$  nm. Dots are measured data and red line represents the fitting curve with Eq. (3). The fitting parameters are listed in Table 1

### 3.2. Device structure

We propose a new device structure to achieve high transmittance using M1. Figure 8(a) and Figure 8(b) depict the cross-sectional and top views of our proposed electrode configuration. The top substrate has a thin surface alignment layer (not shown), while bottom substrate has a planar common electrode, a passivation layer, diamond shaped pixel electrodes, and a thin surface alignment layer (not shown). For simplicity, let us call the structure shown in Figure 8(b) as diamond-shaped FFS mode, abbreviated as d-FFS. The electrode width, electrode gap and electrode tilt angle are denoted as  $w$ ,  $g$  and  $\varphi$ , respectively, and  $\alpha$  is the LC alignment direction (rubbing angle) with respect to  $y$ -axis.

This structure looks similar to traditional stripe structure from cross-sectional view, but it has diamond shape from top view. The reason for making it diamond shape and spatial shift between adjacent pixel electrodes is to increase the transmittance by reducing the dead zones on top of pixel electrodes [66].

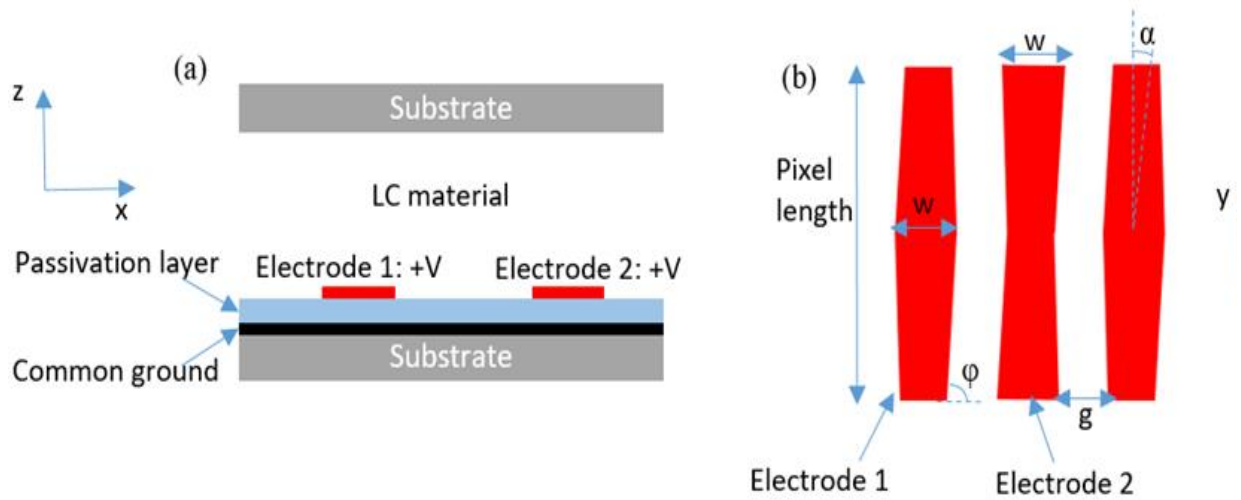


Figure 8 Schematic diagram of the proposed d-FFS structure. (a) Cross-sectional view, and (b) top view.  $w$ : electrode width,  $g$ : electrode gap,  $\varphi$ : electrode tilt angle, and  $\alpha$ : LC alignment direction w.r.t.  $y$  axis.

The LC cell is sandwiched between two crossed linear polarizers. The LC directors are aligned along  $y$ -axis and pretilt angle is  $\theta_p = 0$ . In contrast, the requirement of non-zero pretilt angle in conventional structures limits the tolerable deviation due to rubbing alignment accuracy [56]. Compared to previous report on the interdigitated pixel electrodes of FFS mode, our design significantly boosts the transmittance by reducing the dead zones on top of electrode while maintaining a comparable response time.

### 3.3. Calculated results

We simulated the LC directors distribution of d-FFS cell filled with M1 with a commercial LCD simulator Techwiz LCD 3D (Sanayi, Korea) and then calculated the electro-optic properties by using the extended  $2 \times 2$  Jones matrix method [67]. The parameters employed in the simulation, shown in Figure 8(b), are set as following: LC cell gap  $2.5 \mu\text{m}$ , electrode width  $w=2.0 \mu\text{m}$ , electrode gap  $g=3.0 \mu\text{m}$ , pixel length  $20 \mu\text{m}$ , pixel ITO thickness  $50 \text{ nm}$ , passivation layer thickness  $150 \text{ nm}$ , pretilt angle  $\theta_p = 0$ , and electrode tilt angle  $\varphi=88.85^\circ$ . Anchoring energy of the alignment layer is assumed to be strong. The LC parameters used in this calculation are listed in Table 1. The transmission axis of bottom polarizer is parallel to the LC alignment direction. To explore the tolerance of LC alignment angle, we conducted simulations with two rubbing angles  $\alpha=0^\circ$  and  $1.5^\circ$ ; the former exhibits fast response time due to virtual walls, while the latter exhibits high transmittance owing to the disappearance of virtual walls, as will be explained later.

#### 3.3.1 Voltage-dependent transmittance (VT) curves and response time

To examine at which rubbing angle the virtual walls would disappear, we calculated the response time (rise + decay) time and normalized transmittance at different rubbing angles. Results are plotted in Figure 9. From Figure 9, the transmittance is the lowest and the response time is the fastest when  $\alpha=0^\circ$ , due to the virtual wall effects. These standing exert a strong anchoring force to shorten the LC response time, but the formed dead zones reduce the transmittance significantly.



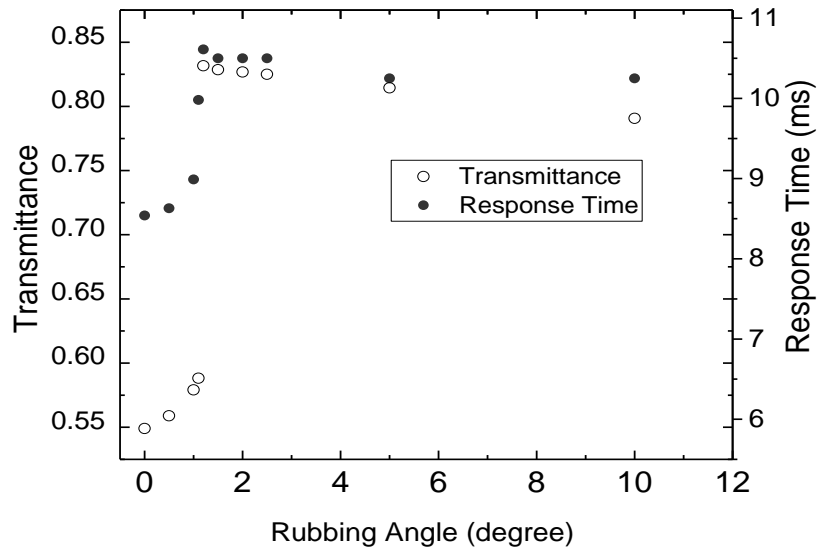


Figure 9 Simulated transmittance and response time of d-FFS at different rubbing angle.

As the rubbing angle increases, the virtual wall effects are gradually weakening. The onset takes place at  $\alpha \approx 1.1^\circ$ ; above  $\alpha \approx 1.2^\circ$ , the transmittance increases sharply but the response time also increases. As  $\alpha > 1.5^\circ$ , the transmittance starts to decline gradually (due to decreased phase retardation) while response time remains more or less unchanged. Therefore, the optimal rubbing angle lies between  $1.2^\circ$  and  $2.0^\circ$ .

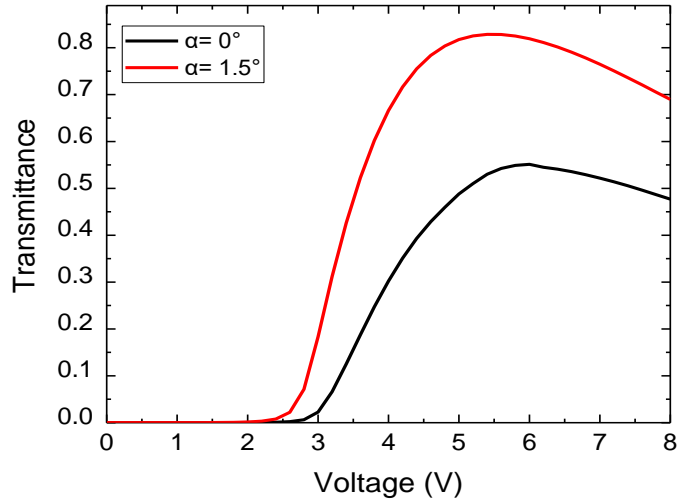


Figure 10 Simulated VT curves of d-FFS at  $\alpha = 0^\circ$  and  $1.5^\circ$ ,  $\lambda = 550$  nm.

Figure 10 shows the simulated voltage-dependent transmittance (VT) curves at  $\alpha = 0^\circ$  and  $\alpha = 1.5^\circ$ , while keeping the LC pretilt angle at  $\theta_p = 0^\circ$ . At  $\alpha = 0^\circ$ , the peak transmittance (at  $5.8 V_{\text{rms}}$ ) is 54.9%. Although the transmittance is relatively low, this result is comparable to those reported in [21]-[23]. Indeed, this is a general trade-off between response time and transmittance. However, the result at  $\alpha = 1.5^\circ$  is quite unexpected. Its peak transmittance reaches  $\sim 82.9\%$  at  $5.4 V_{\text{rms}}$ . Detailed physical mechanism will be discussed later. The increased peak transmittance is particularly desirable for high-resolution-density displays, where the aperture ratio and optical efficiency are both decreased. As will be discussed later, low backlight duty-ratio can be applied to shorten the motion picture response time (MPRT) to 1.5 ms. However, the trade-off is decreased display luminance. Therefore, the high-transmittance d-FFS LCD offers a promising solution for suppressing image blurs while

keeping a relatively high display luminance. The latter is particularly important for the battery-powered mobile display devices.

Low viscosity is helpful for achieving fast response time. As listed in Table 1, M1 exhibits a very low rotational viscosity ( $\gamma_1=35.75$  mPas). Figure 11 shows the calculated time dependent transmittance curves for d-FFS at  $\alpha=0^\circ$  and  $1.5^\circ$ . The voltage corresponding to peak transmittance is applied to calculate the rise time and decay time. Response time is defined as the transmittance change between 10% and 90% of the maximum value.

At  $\alpha=0^\circ$ , the rise time and decay time are calculated to be 5.59 ms and 2.95 ms, whereas at  $\alpha=1.5^\circ$  the rise time and decay time are 5.75 ms and 4.75 ms. At  $\alpha=0^\circ$ , the observed faster decay time results from the restoring force exerted by the virtual walls.

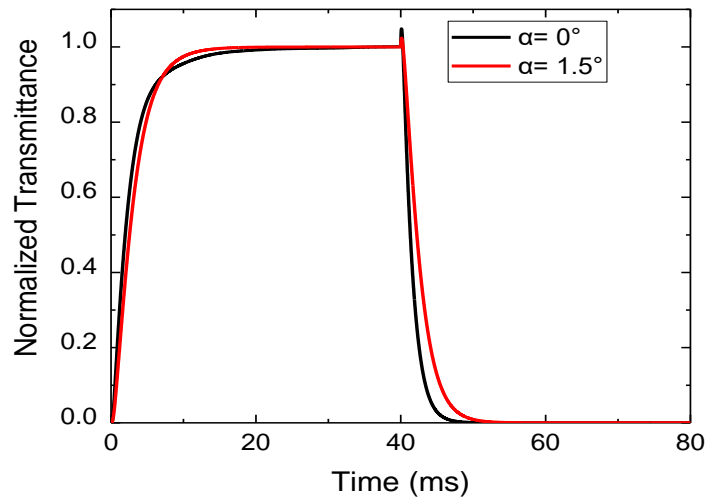


Figure 11 Simulated response time curves of d-FFS at  $\alpha=0^\circ$  and  $1.5^\circ$ .

In comparison, the response time of our d-FFS is faster than that of the alternating tilt device under the same rubbing angle [56] because of its slightly thinner cell gap. Our d-FFS at  $\alpha=1.5^\circ$

offers  $\sim 85\%$  transmittance (normalized to that of two parallel polarizers) and reasonably fast response time. Such a high transmittance is comparable to that of a single-domain FFS mode with a positive  $\Delta\epsilon$  LC, but the average GTG response time is about 2x faster [68].

### 3.3.2 Electrode structure optimization

To find the optimal device parameters, we perform simulation with different electrode width and electrode gap for the d-FFS LCD with  $\alpha=1.5^\circ$ . Figure 12(a) shows the simulated VT curves when electrode width ( $w$ ) varies from  $2.0\ \mu\text{m}$  to  $4.0\ \mu\text{m}$ , while keeping electrode gap ( $g$ ) at  $3.0\ \mu\text{m}$ .

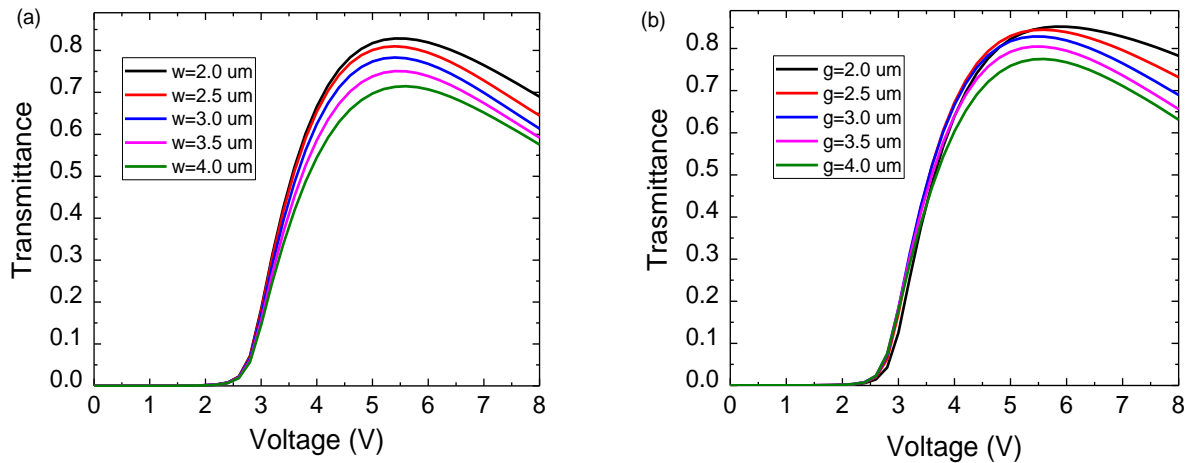


Figure 12 Simulated VT curves of d-FFS using M1. (a) Keeping electrode gap at  $3.0\ \mu\text{m}$  while varying electrode width from  $2.0\ \mu\text{m}$  to  $4.0\ \mu\text{m}$ . (b) Keeping electrode width at  $2.0\ \mu\text{m}$  while varying electrode gap from  $2.0\ \mu\text{m}$  to  $4.0\ \mu\text{m}$ .

As Figure 12(a) depicts, the peak transmittance decreases gradually as the electrode width increases from  $2.0\ \mu\text{m}$  to  $4.0\ \mu\text{m}$  due to the enlarged dead zone area. However, the on-

state voltage only slightly shifts from 5.4V to 5.6V, as it is less sensitive when a small  $\Delta\epsilon$  LC is employed [69].

Figure 12(b) shows the simulated VT curves where electrode gap varies from 2.0  $\mu\text{m}$  to 4.0  $\mu\text{m}$  while keeping electrode width at 2.0  $\mu\text{m}$ . As the electrode gap increases, transmittance decreases because more LC directors at the center of electrode do not reorient.

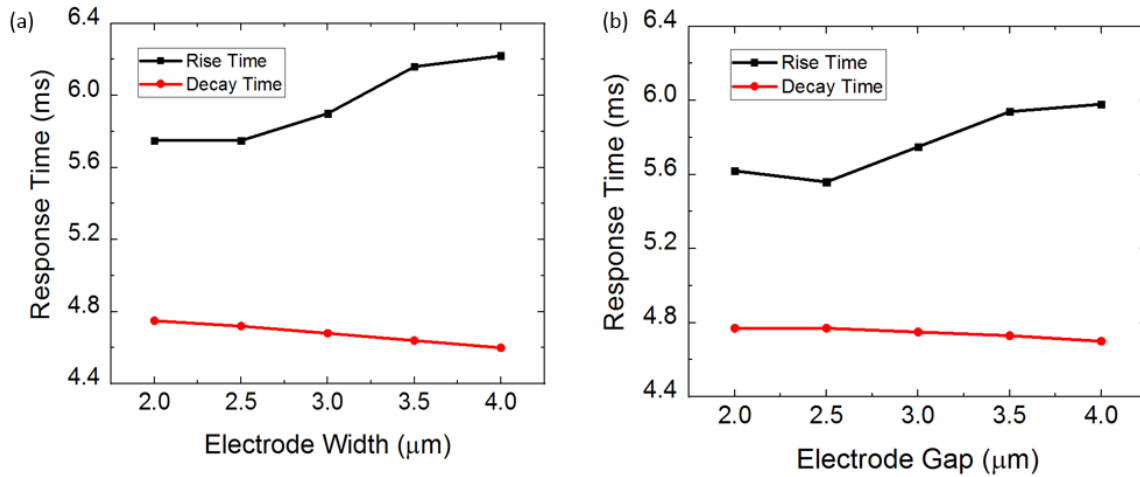


Figure 13 Calculated response time for p-FFS using UCF-M2 (a) Keeping gap 3.0  $\mu\text{m}$  while varying width from 2.0  $\mu\text{m}$  to 4.0  $\mu\text{m}$  (b) Keeping width 2.0  $\mu\text{m}$  while varying gap from 2.0  $\mu\text{m}$  to 4.0  $\mu\text{m}$

Figure 13 shows the response time of our liquid crystal device with different electrode width and electrode gap at corresponding maximum voltage. From Figure 13(a), when electrode width increases at constant gap, rise time increases while decay time decreases. We are observing the same trend of increasing rise time when gap between electrode increases at constant width while decay time doesn't change too much. When electrode gap increases, liquid crystal molecule near to the center receives weaker fringe

electric field resulting in slower average rising time. For the d-FFS with  $w=2.0\ \mu\text{m}$  and  $g=2.0\ \mu\text{m}$ , the simulated peak transmittance is 85.2%, rise time  $\approx 5.62\ \text{ms}$ , and decay time  $\approx 4.77\ \text{ms}$  at  $V_{\text{on}} = 5.8V_{\text{rms}}$ .

Table 2 Calculated peak transmittance and response time at the on voltage for 3 LC devices

<b>LC Device</b>	Rubbing angle	Voltage (V)	Transmittance	Rise (ms)	Decay (ms)
<b>Device I</b>	0°	5.0	47.0%	5.9	3.2
	1.5°	5.2	69.5%	7.0	6.1
<b>Device II</b>	0°	6.6	47.0%	5.2	2.5
	1.5°	6.4	79.4%	6.7	4.7
<b>Proposed device</b>	0°	6.2	51.1%	5.0	2.4
	1.5°	5.8	85.2%	5.6	4.8

Table 2 compares the performance of our proposed device with two prior LC devices: Device I and Device II. The goal of this analysis is to distinguish the improvement from material and device structure. For Device I, a positive  $\Delta\epsilon$  LC material and interdigitated pixel electrode structure with alternative tilt are used [56]. Device II has the same configuration as Device I, except that the employed LC material is replaced by our M1 mixture. For a fair comparison, we use the same electrode width ( $2.0\ \mu\text{m}$ ), electrode gap ( $2.0\ \mu\text{m}$ ) and cell gap ( $2.5\ \mu\text{m}$ ). While comparing Device II with Device I, we find that the rise time and decay time are all reduced for both  $\alpha=0^\circ$  and  $\alpha=1.5^\circ$ . This is because M1 has a lower viscosity (35.75 mPas vs. 47.6 mPas). Moreover, for the case of  $\alpha=1.5^\circ$ , the transmittance of Device II is higher than that of Device I (79.41% vs. 69.52%). The enhanced transmittance is the product of

smaller  $\Delta\epsilon$  [59] and higher  $\epsilon_{\perp}/\epsilon_{\parallel}$  ratio [60] of our M1 mixture. However, a major tradeoff is increased on-state voltage because M1 has a smaller  $\Delta\epsilon$  (2.66 vs. 5.1) in Device II. When comparing our proposed device with Device II (using the same M1 mixture), we find the improvement is in three areas: 1) the transmittance is improved from 79.4% to 85.2%, 2) the on-state voltage is decreased from 6.4V to 5.8V, and 3) the response time (rise + decay) is slightly faster (from 11.4 ms to 10.4 ms). The lower operation voltage is due to the electrode shape and uniform tilt and twist angles of LC directors in the voltage-on state.

### **3.4. Discussion**

In order to get high transmittance, fast response time, and low operation voltage, we have introduced an improved mixture to our d-FFS mode. Our LC material exhibits a low viscosity which helps to reduce response time. However, the trade-off is its low  $\Delta\epsilon$ , which leads to increased operation voltage. With our diamond-shape electrodes, we are able to keep a high transmittance ( $\sim 85\%$ ) at 5.8V. To lower the operating voltage to 5V (similar to that of most commercial LCDs), we need to increase  $\Delta\epsilon$  by  $\sim 35\%$ , which would slightly increase the viscosity. It is worth mentioning that the electric field in our d-FFS mode is at an oblique angle to the LC directors, which eliminates the requirement of non-zero pretilt angle for forming two-domain LC confinement. Figure 14(a) and Figure 14(b) shows the cross-sectional view of LC director configuration and the corresponding transmittance at a voltage-on state for  $\alpha=0^\circ$  and  $\alpha=1.5^\circ$ , respectively. In Figure 14(a), because the rubbing angle is zero, the virtual walls above the electrodes provide additional restoring force to the LC directors. Hence, fast response is obtained. However, dead zones are formed at the same

time, leading to a relatively low transmittance. To boost transmittance, we investigated the device configuration with  $\alpha=1.5^\circ$ . As Figure 14(b) depicts, the LC directors above the electrodes are also reoriented by the electric field, which reduces the dead zone area. In addition, the spatial shift between adjacent pixels and common electrodes helps to spread the electric field more uniformly, which also contributes to the increased transmittance. Our d-FFS with  $\alpha=1.5^\circ$  rubbing angle is very preferable in terms of transmittance while the tradeoff in response time is minimal. In the following sections, we will show the calculated gray-to-gray (GTG) response time, MPRT, viewing angle, gamma shift, and color shift for our d-FFS at  $\alpha=0^\circ$  and  $\alpha=1.5^\circ$  rubbing angle with optimized structure.

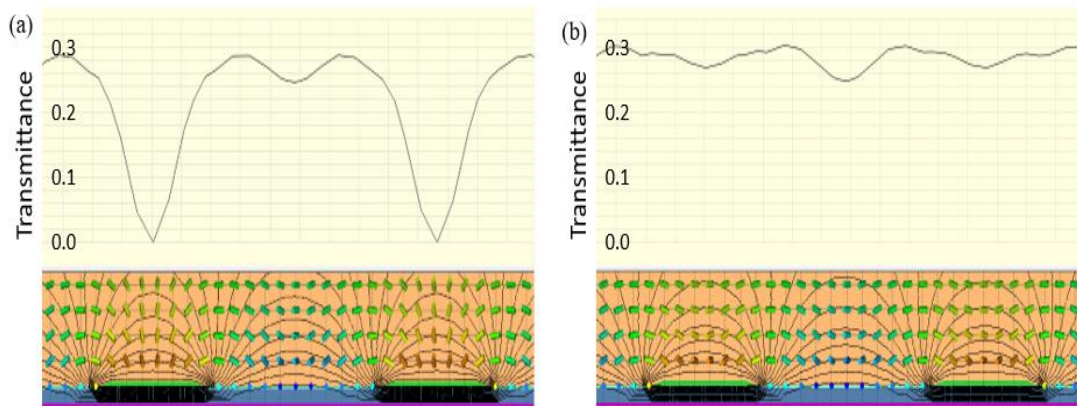


Figure 14 Cross-sectional view of the simulated LC director distributions and local relative transmittance of d-FFS cell at (a)  $\alpha=0^\circ$ , and (b)  $\alpha=1.5^\circ$  rubbing angle.



### 3.4.1 Gray-to-gray (GTG) response time

We divide the VT curve uniformly into 256 gray levels based on gamma-2.2 rule in order to obtain the response time between different gray levels. We study the transitions between 0, 64, 128, 192 and 255 gray levels. The GTG response time (rise and decay) is defined between 10% and 90% transmittance change. The simulated GTG response times are listed in Table 3 and 4 for  $\alpha=0^\circ$  and  $\alpha=1.5^\circ$ , respectively. From Table 3 and Table 4, the average GTG response time is found to be 5.35 ms for  $\alpha=0^\circ$ , and 8.81 ms for  $\alpha=1.5^\circ$ . The faster average GTG response time for  $\alpha=0^\circ$  is expected because of the virtual walls. However, its transmittance is greatly sacrificed.

Table 3 Calculated GTG response time (ms) of our proposed d-FFS with  $\alpha=0^\circ$ .

<b>Voltage</b>	0 V	3.08 V	3.46 V	4.04 V	6.20 V
<b>Gray Level</b>	<b>0</b>	<b>64</b>	<b>128</b>	<b>192</b>	<b>255</b>
<b>0</b>		13.19	8.5	5.42	4.95
<b>64</b>	1.93		7.66	5.12	4.37
<b>128</b>	1.97	8.12		4.69	4.49
<b>192</b>	2.08	6.12	5.31		4.67
<b>255</b>	2.43	5.85	5.68	4.44	

Table 4 Calculated GTG response time (ms) of our proposed d-FFS with  $\alpha=1.5^\circ$ .

<b>Voltage</b>	0 V	2.75 V	3.10 V	3.55 V	5.80 V
<b>Gray Level</b>	<b>0</b>	<b>64</b>	<b>128</b>	<b>192</b>	<b>255</b>
<b>0</b>		16.15	14.70	11.56	5.62
<b>64</b>	3.85		10.69	10.52	5.31
<b>128</b>	4.02	11.19		9.49	5.09
<b>192</b>	4.19	12	10.67		5.31
<b>255</b>	4.77	11.76	10.45	8.98	

To evaluate image blurs of a TFT-LCD or OLED, motion picture response time (MPRT) should be considered. For a TFT-LCD, its MPRT depends on the LC response time and TFT frame rate as [14]:

$$MPRT \approx \sqrt{\tau^2 + (0.8 \times T_f)^2}. \quad (4)$$

In Eq. (4),  $\tau$  is the LC response time and  $T_f (=1000/f)$  is the TFT frame time. Based on Eq. (4), if the FFS device is driven at 144 Hz, then its corresponding average GTG MPRT should be 7.82 ms and 10.41 ms at  $\alpha=0^\circ$  and  $\alpha=1.5^\circ$ . Both are too slow and image blur would be inevitable. To suppress image blurs to unnoticeable level, we set CRT-like MPRT as the criterion, which is 1.5 ms. From Eq. (4), if  $\tau \approx 5$  ms, then it is impossible to reduce the MPRT to 1.5 ms, even we increase the frame rate. Another drawback for increasing frame rate is the dramatically shortened TFT charging time, especially for a high-resolution (4K2K) display. A more effective way to reduce MPRT is to decrease the duty ratio [70], [71].

Especially, when the duty ratio is low, MPRT is less sensitive to the LC response time. This is because the backlight is turned-on at later stage so that the beginning slow response is more forgiven. However, decreasing the duty ratio would lower the display luminance proportionally. Table 5 shows the required duty ratio and resultant display transmittance in order to obtain MPRT= 1.5 ms at 90-Hz and 120-Hz frame rates for  $\alpha=0^\circ$  and  $\alpha=1.5^\circ$ . From Table 5, at 90 Hz we need to reduce the duty ratio to 17% for both  $\alpha=0^\circ$  and  $\alpha=1.5^\circ$  in order to obtain MPRT=1.5 ms. Under such a circumstance, the corresponding effective transmittance is 0.086 for  $\alpha=0^\circ$  and 0.144 for  $\alpha=1.5^\circ$ . That means, the device with  $\alpha=1.5^\circ$  exhibits a 67% higher transmittance than that with  $\alpha=0^\circ$ . Similar improvement (67%) in transmittance is also found at 120-Hz framerate. This is why the high transmittance of our proposed FFS device with  $\alpha=1.5^\circ$  is so much more favorable than that with  $\alpha=0^\circ$ , although the latter has a faster response time.

Table 5 Calculated GTG response time (ms) of our proposed d-FFS with  $\alpha=1.5^\circ$ .

<b>Rubbing angle</b>	<b>LCD Trans. (%)</b>	<b>MPRT (ms)</b>	<b>Backlight on-time (ms)</b>	<b>LC response time (ms)</b>	<b>Frame rate (Hz)</b>	<b>Frame time (ms)</b>	<b>Duty ratio</b>	<b>Effective Trans. (%)</b>
<b>0°</b>	51.1	1.50	1.88	5.35	90	11.1	0.17	8.6
	51.1	1.50	1.88	5.35	120	8.3	0.23	11.5
<b>1.5°</b>	85.2	1.50	1.88	8.81	90	11.1	0.17	14.4
	85.2	1.50	1.88	8.81	120	8.3	0.23	19.2

### 3.4.2 Viewing angle

As Figure 8(b) shows, the gaps (white areas) between electrodes exhibits zig-zag structure. That means, each pixel actually exists multi-domain structure, which helps to widen the viewing angle. We use a positive A-plate and a positive C-plate as compensation films. Their refractive indices and film thickness are listed as follows:  $n_{e,+A} = 1.5110$ ,  $n_{o,+A} = 1.5095$ ,  $n_{e,+C} = 1.5110$ ,  $n_{o,+C} = 1.5095$ ,  $d_{+A} = 92.59 \mu\text{m}$ , and  $d_{+C} = 60.09 \mu\text{m}$ . Figure 15(a) and Figure 15(b) depict the simulated isocontrast contour of our d-FFS LCD with compensation films at  $\alpha=0^\circ$  and  $\alpha=1.5^\circ$ , respectively. For  $\alpha=1.5^\circ$ , maximum contrast ratio over 5000:1 is obtained and it expands to a larger zone when compared to  $\alpha=0^\circ$  where maximum contrast ratio is 3357:1. In both cases, the contrast ratio over 500:1 expands to  $\sim 70^\circ$  viewing cone and it remains over 100:1 in the entire viewing cone.

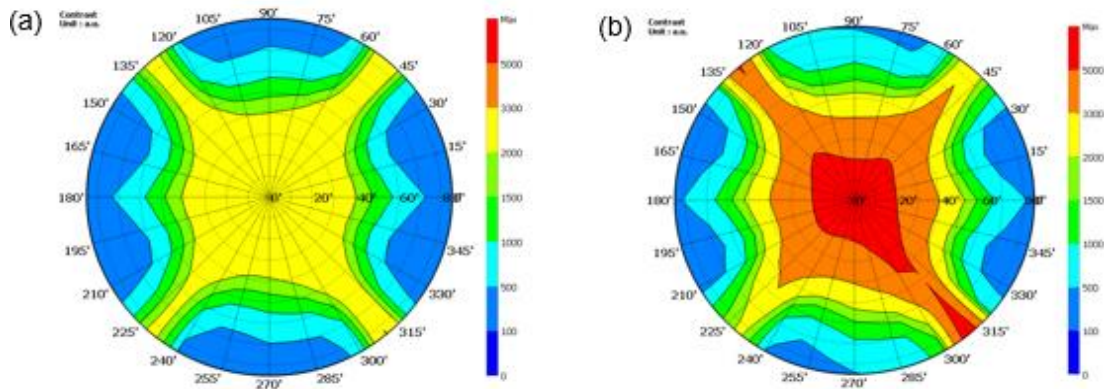


Figure 15 Simulated isocontrast contour of d-FFS LCD with (a)  $\alpha=0^\circ$  (b)  $\alpha=1.5^\circ$  using a positive A-plate and a positive C-plate.

### 3.4.3 Gamma curve

In addition to high transmittance, fast MPRT, and wide viewing angle, small gamma shift is also critically important for a display device. To quantify gamma shift, an off-axis image distortion index (D) has been defined [72].

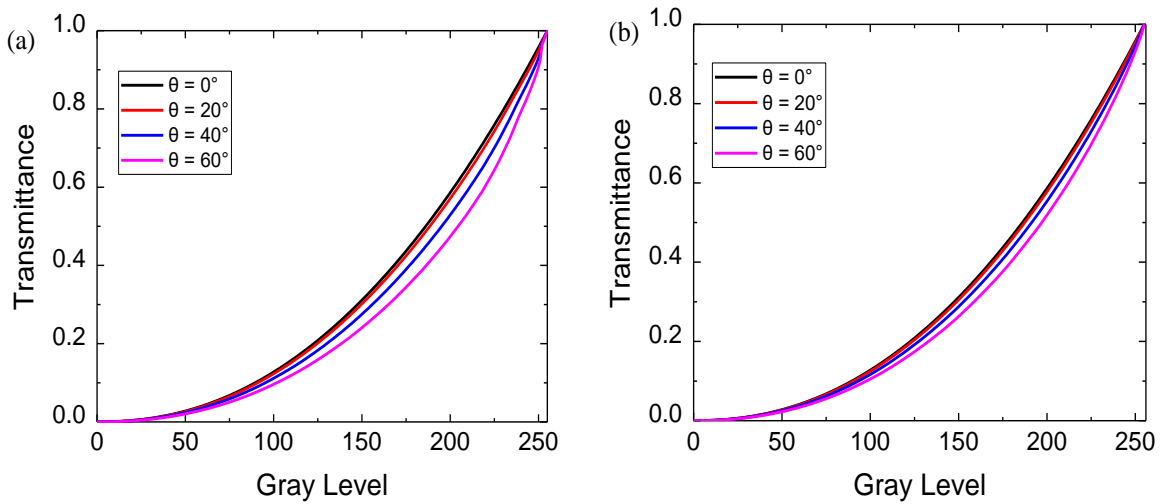


Figure 16 Simulated gamma shift of the film-compensated d-FFS LCD at (a)  $\alpha=0^\circ$  and (b)  $\alpha=1.5^\circ$ .

Figure 16(a) and Figure 16(b) show the simulated gamma curves of our d-FFS LCD at four specified viewing angles for  $\alpha=0^\circ$  and  $\alpha=1.5^\circ$ , respectively. Along the  $0^\circ$  azimuthal angle, we find  $D(60^\circ, 0^\circ) = 0.182$  for  $\alpha=0^\circ$  and  $D = 0.113$  for  $\alpha=1.5^\circ$ . In both scenarios, D is smaller than 0.2, which means the gamma shift of our d-FFS LCD is indistinguishable by the human eye [73].

### 3.4.4 Color shift

Indistinguishable color shift is another critical requirement of all display devices. By using a quantum dot enhancement film [74], [75], we calculated the color shift of our d-FFS

LCD at different viewing angles. Color shift in  $\Delta u'v'$  color coordinate system at different polar angles (at  $0^\circ$  azimuthal angle) are shown in Figure 17(a) and Figure 17(b) at  $\alpha=0^\circ$  and  $\alpha=1.5^\circ$ , respectively. From Figure 17, the color difference for RGB wavelengths is smaller than 0.008 even at  $\sim 80^\circ$  viewing cone. When  $\Delta u'v'$  is smaller than 0.02, it is indistinguishable to the human eye.

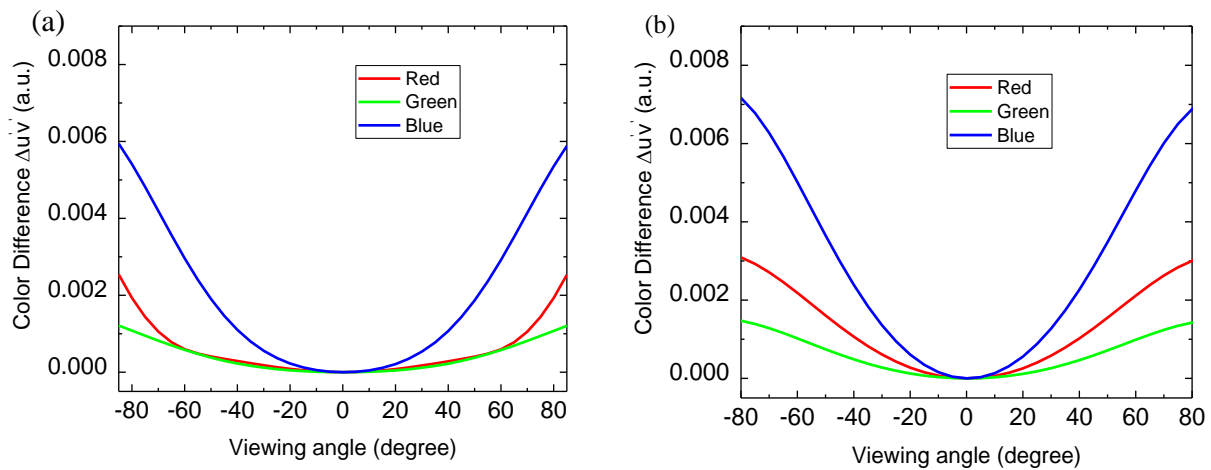


Figure 17 Simulated color shift at (a)  $\alpha=0^\circ$  (b)  $\alpha=1.5^\circ$  using a quantum dot-enhanced backlight.

### 3.5. Summary

We have reported a positive  $\Delta \epsilon$  LC mixture and a diamond-shape pixel configuration for FFS mode. High transmittance ( $T_{\max} \sim 85\%$ ), fast response time, and low operation voltage (5.8V) have been achieved. High transmittance and fast LC response time are critical for high resolution density and high frame rate displays to keep low power consumption and to mitigate image blurs. We have also achieved high contrast ratio, wide view, and indistinguishable color shift and gamma shift by using compensation films. Considering

these outstanding features, our proposed d-FFS LCD should have potential for many practical applications.

## CHAPTER 4: PHOTO-RESPONSIVE LIQUID CRYSTAL DIMMER

In this section, a new guest-host photosensitive cholesteric liquid crystal (CLC) smart dimmer will be demonstrated. Black dichroic dye is used as a guest in host liquid crystal material with chiral agent. This dimmer can be used for enhancing the ambient contrast ratio of augmented reality displays. In the experiment section, method of formulating this mixture and characterization will be explained. Mechanism of our smart dimmer will be discussed and experimental results will also be shown.

### 4.1. Experiment

A negative dielectric anisotropy ( $\Delta\epsilon$ ) nematic mixture Merck ZLI-4788 was used as the LC host for this experiment. Its physical properties are listed as follows:  $\Delta\epsilon = -5.7$  at  $f = 1$  kHz and birefringence  $\Delta n = 0.1647$  at  $\lambda = 589$  nm. A right-handed photosensitive chiral azobenzene compound, PSC-01 [76], [77], was doped into this LC host.

The HTP of PSC-01 in trans and cis state is  $64.18 \mu\text{m}^{-1}$  and  $16.31 \mu\text{m}^{-1}$ , respectively. Figure 18 shows the chemical structure of PSC-01. Next, we added a left-handed chiral agent, Merck

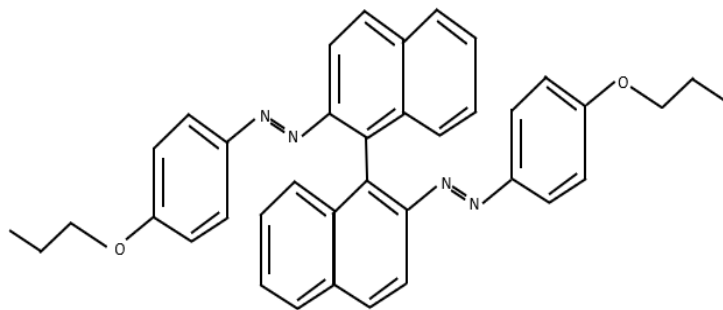


Figure 18 Chemical structure of PSC-01



S-811, to the mixture. The concentration of PSC-01 and S-811 is 0.7 wt% and 3.8 wt%, respectively. Different concentration of black dichroic dye S428 (Mitsui, Japan) was incorporated into the mixture. After accurate weighing and mixing of components, the mixtures were heated to an isotropic phase and stirred for several minutes in order to dissolve fully. Then, the prepared sample mixture was filled into a LC cell, comprising of two glass plates. The cell gap was measured to be 9.1  $\mu\text{m}$ . The glass surface was spin-coated with a thin polymer layer to align the injected CLC mixture perpendicular to the glass substrates. The cell was then cooled down slowly to the room temperature ( $\sim 23^{\circ}\text{C}$ ). In this experiment, we used two commercial light sources (UV and blue light) to irradiate the LC sample. The UV light source was Darkbeam UV365 LED lamp, whose central wavelength is 365 nm and FWHM (full-width at half-maximum) is 7 nm. The blue light source is a blue LED whose central wavelength is 450 nm. For the reversal process, we used a He-Ne laser beam whose wavelength is 633 nm. We used Deuterium halogen light source (DH-2000) and HR4000CG-UV-NIR spectrometer (Ocean Optics) to measure the spectrum and time dependent transmittance curve for our prepared cell before and after exposure. Microscopic images of our sample in both states were taken using Olympus BX51 polarizing optical microscope.

## **4.2. Mechanism**

The trans-azobenzene compounds (Figure 18) dissolve well into ZLI-4788 without significantly disorganizing the molecular orientation of the LC host because the shape of this trans-molecule is similar to the nematic host. When the right-handed chiral azobenzene molecule is exposed to UV-blue light, it undergoes trans-cis photoisomerization. The UV-blue

light exposure transforms the rod-shaped (trans-state) azobenzene molecule into higher energy kinked shape (cis-state). Such a higher energy kink-shaped cis-state can be transformed back to the original rod-shaped trans-state upon exposure to visible light or heat [78]-[81]. The helical twist power of this right-handed chiral compound doped LC host depends on the photoisomerization state. The trans-cis photoisomerization of chiral azobenzene compounds decrease the helical twist power. Chiral dopant structure and the molecular interaction between chiral dopant and nematic LC host control this helical twist power. A left-handed chiral dopant S-811 was added to cancel the helical twisting power of trans-PSC-01. Therefore, in the initial state, there is no twist in the structure. Because the LC mixture is in vertical alignment, its initial state transmittance is the highest, i.e. lowest dye absorption. Upon photo-isomerization of blue/UV irradiation, a portion of trans-PSC-01 is promoted to cis-PSC-01 (lower helical twist power) while S-811 is unaffected. Thus, the overall helical twisting power is left-handed. The pitch length (P) of LC directors depends on the chiral concentration (C) and helical twisting power ( $\beta$ ). In experiment, the pitch length can be approximated as  $P=1/(C.\beta)$  [76]. The enhanced overall helical twisting power of the mixture will shorten the helical pitch value of the LC directors. In a given cell, a certain minimal pitch value can be achieved as  $P_{th}=2dK_{22}/K_{33}$  where  $K_{22}$  and  $K_{33}$  are the elastic constants for twist and bend deformations, respectively [82]. As in the photo-isomerization state, P is smaller than  $P_{th}$ , and the twisted cholesteric structure (fingerprint) is achieved due to the strong torque, which is larger than the elastic torque determined by orientational elasticity and anchoring. This leads to decreased transmittance due to dye absorption and scattering from the cholesteric directors. In the reversal process, when the sample is

irradiated with a red light, cis-trans back isomerization of PSC-01 takes place and the increased helical twist power of trans-PSC-01 cancels out the left-handed twist power of S-811. Therefore, the overall twist power of the mixture decreases while P increases. When P is larger than the critical pitch, the chiral torque is too weak and the LC is reversed back to the initial (homeotropic) state. Thus, the cell become transparent again due to the minimal absorption and scattering.

### **4.3. Results and discussion**

Figure 19 depicts the structures and mechanism of our proposed photosensitive device. Figure 19(a) shows the distribution of LC directors and dichroic dyes in the structure when unexposed to UV-blue light. At this state, the LC directors and dyes are perpendicularly aligned to the glass substrate. For a dichroic dye, if the incident light polarization is parallel to the longer molecular axis, such a polarized light would be absorbed strongly. On the contrary, if the light's polarization is perpendicular to the dyes long axis, the absorption is much weaker. Hence, the transmittance is high. In our experiment, when the prepared cell is exposed to UV-blue light, isomerization takes place and the LC directors are reoriented from homeotropic state to fingerprint state, as Figure 19(b) shows. Because of the doped chiral agent S811, the LC directors and dye molecules form cholesteric helical structure, where the helical axis is parallel to the substrate. Under such a condition, the dye molecules can absorb light polarized along the same axis. In addition, the light polarized perpendicular to the LC directors will still be absorbed slightly because the limited dichroic ratio of the dye molecules. In the cholesteric state, the orientation, which allows part of the directors to be

perpendicular to the boundary, is the texture where the helix axis is parallel to the surface. In this state, the device not only absorbs (by the dye molecules) but also scatters the incident light (by the LC directors), resulting in a low transmittance. Unlike a traditional guest-host system, our proposed photo-switchable device only consumes power during dynamic switching and is stable in the absence of irradiation.

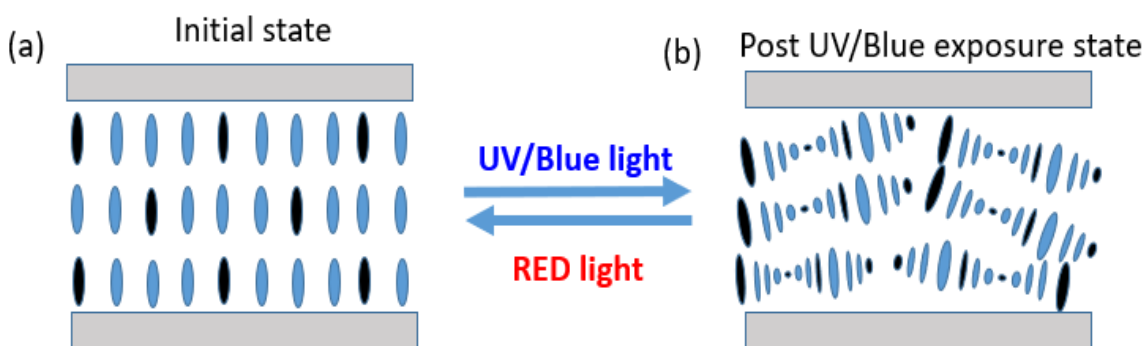


Figure 19 LC director and dye orientations of the proposed photo-sensitive dimmer.

The reversal process from fingerprint state to vertical state can be carried out either by a longer wavelength light exposure or by heat. We measured the transmission spectra of our sample from 400 nm to 700 nm at the room temperature (23°C). Results are depicted in Figure 20 for the sample containing 2wt% dichroic dye before and after UV exposure. At initial state (Figure 20(a)), a relatively high transmittance (60-70%) is obtained in the visible spectral region because the absorption loss is minimal. The remaining optical loss is due to limited dichroic ratio of the employed dyes and order parameter, and surface reflections. As shown in Figure 20, transmittance decreases significantly in the visible region after UV exposure. At  $\lambda=550$  nm, transmittance drops from 65.6 % to 17.4% when the UV lamp was

turned on. The LC directors and dyes are in fingerprint state at post exposure state as Figure 20(b) depicts. As dichroic dye and LC directors are in fingerprint state, the LC cell turned into dark due to the absorption and scattering. The measured contrast ratio is about 4:1, which is quite typical for a guest-host display.

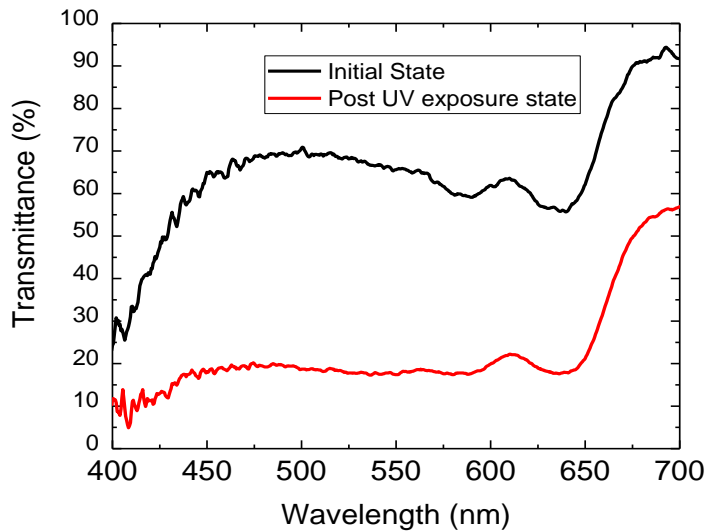


Figure 20 Measured transmission spectra of our LC sample before and after UV exposure.

Figure 21 shows the images behind our photosensitive LC device before and after UV exposure. The dynamic transition is recorded in Visualization 1. The images were taken under the lab yellow lighting environment. When the sample is not exposed to UV light (Figure 21(a)), we can easily recognize the colored “UCF” because our dimmer is a broadband device. After UV exposure (Figure 21(b)), the transmittance decreases but the image of “UCF” remains distinguishable because the transmittance stays at about 15-20%. The intermediate transmittance state can be achieved by controlling the UV dosage. Thus, this passive dimmer does not need an adaptive sensor and this is an important advantage of

our device. Under strong UV light illumination, it gets darker. When the UV light is weak, the device becomes transparent. No sensor is needed which is similar to a photochromic glass.

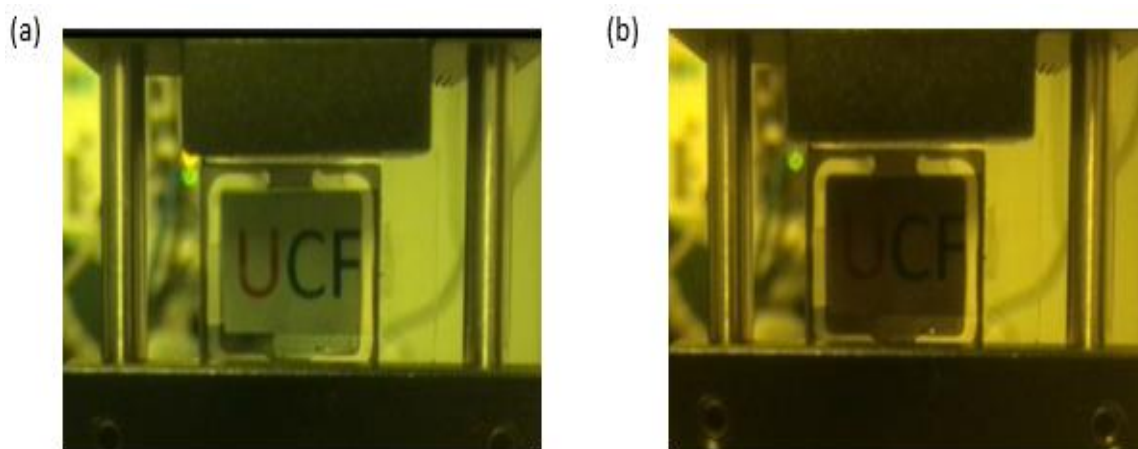


Figure 21 See-through image of our smart dimmer: (a) before and (b) after UV exposure.

The switching time of our photosensitive guest-host device depends on the light dosage. Figure 22 shows the measured transmittance change ( $\lambda=550$  nm) as the UV exposure time increases. In Figure 22, the red line represents the measured transmittance when the sample is exposed to a weak UV light ( $\lambda=365$  nm and intensity  $\approx 0.12$  mW/cm<sup>2</sup>), whereas black line shows the measured result using a strong UV light (intensity  $\approx 0.5$  mW/cm<sup>2</sup>). As the black line depicts, the transmittance declines from  $\sim 65.6\%$  to  $\sim 23\%$  at about 8s. Although slow, this result is comparable with commercial photochromic transition glass [24], [83]. But when the sample is exposed to a weak UV light, the response time becomes slower, which takes 13.5s to drop to  $\sim 23\%$  transmittance. As the UV light intensity increases, the number of photons increases, so does the probability of photo-chemical reaction. As a result, the turn-

on time is faster. The response time can be further improved by using a faster azobenzene material [84].

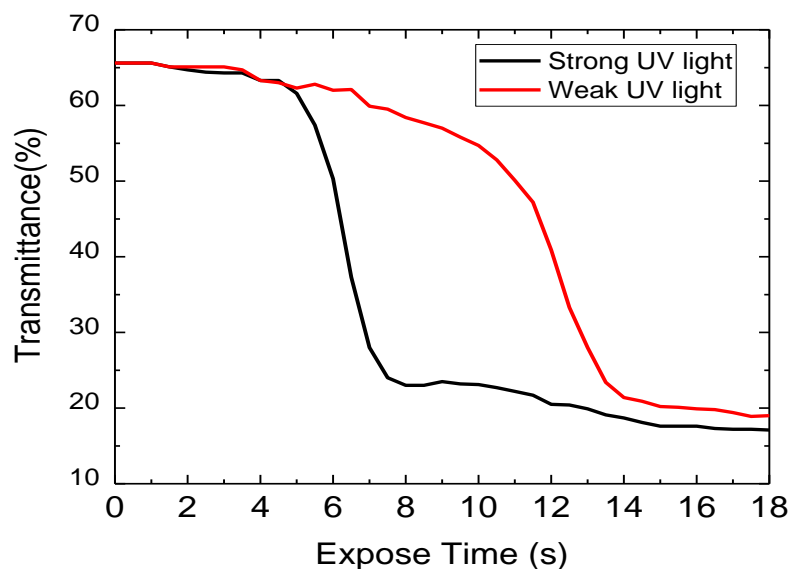


Figure 22 Measured transmission vs. exposure time (UV light).

In addition to UV light, we also irradiated blue light to our guest-host CLC sample and measured the dynamic response. Results are plotted in Figure 23, where the red line corresponds to the measured result for a strong blue light irradiation ( $\lambda \approx 450$  nm and intensity =  $2.57 \text{ mW/cm}^2$ ) and black line represents a weak blue light exposure (intensity =  $0.57 \text{ mW/cm}^2$ ). From Figure 23, it takes 16s to decrease the transmittance from  $\sim 65.6\%$  to  $\sim 23\%$  for a strong blue light exposure. This response time is longer than the corresponding UV light. For a weaker blue light exposure, the response time is even longer ( $\sim 21$ s). This means, our smart dimmer can be activated by either UV light or blue light, depending on the application needs. This is particularly important for vehicle displays because the majority of UV light is blocked by the windshield. Therefore, the commercial transition glass does not

function well inside a car. Our CLC dimmer can be activated by blue light. Thus, it works inside a vehicle.

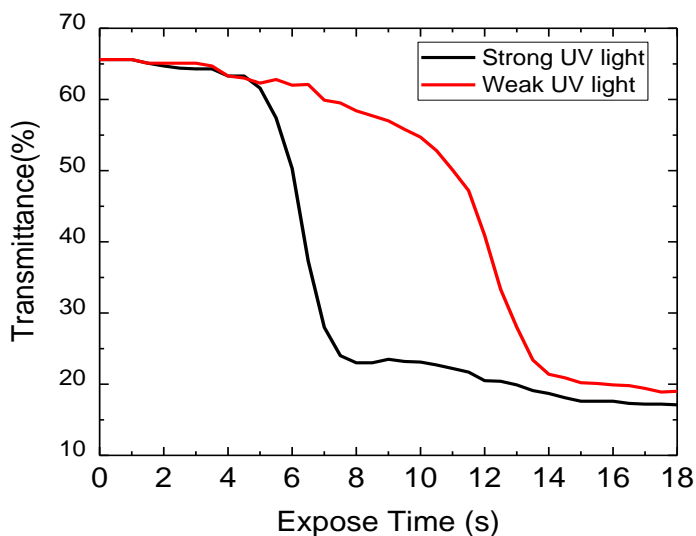


Figure 23 Measured transmission vs. exposure time using a blue light  $\lambda \approx 450$  nm.

In order to measure the reversal time, we exposed our guest-host device using a red He-Ne laser beam ( $\lambda = 633$  nm and intensity =  $6.8$  mW/cm<sup>2</sup>) at the post UV exposure state. In Figure 24, we plot the transmittance change with respect to the laser exposure time. From Figure 24, it takes  $\sim 42$ s to change the transmittance from  $\sim 20.7\%$  to  $\sim 53.8\%$ . Such a sluggish response time is due to the slow cis-trans transition of the employed chiral azobenzene molecules.



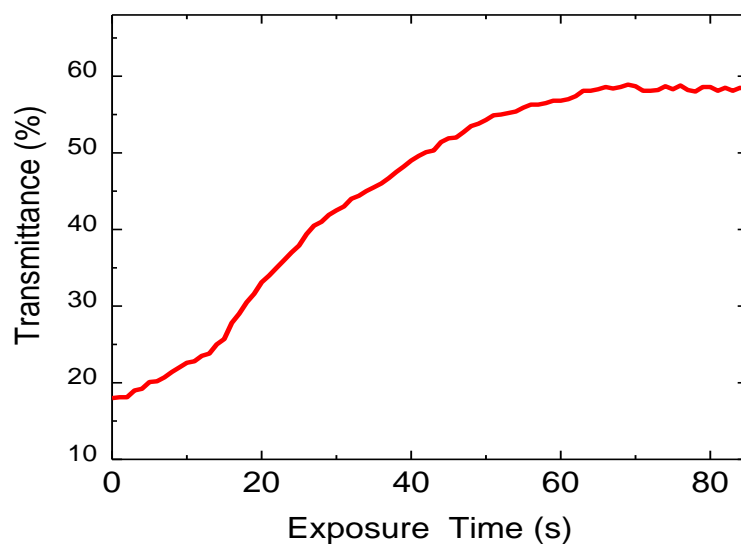


Figure 24 Measured transmission vs. exposure time of reversal process using a red HeNe laser beam.

Next, we investigate how the dichroic dye concentration affects the transmittance and contrast ratio of our samples. To do so, we prepared four samples, S1-S4, by varying the S428 dye concentration from 2% to 3.5%. Table 6 lists the detailed concentration of each compound.

Table 6 Prepared 4 samples using different dichroic dye (S428) concentration

Sample	S428 (wt%)	ZLI-4788 (wt%)	S-811(wt%)	PSC-01(wt%)
S1	2.0%	93.4%	3.8%	0.8%
S2	2.5%	92.9%	3.8%	0.8%
S3	3.0%	92.4%	3.8%	0.8%
S4	3.5%	91.9%	3.8%	0.8%

We characterized the transmittance of these four samples (S1-S4) before and after UV exposure. Figure 25(a) shows the measured transmittance (at  $\lambda=550$  nm) versus S428 concentration before and after UV exposure. As expected, transmittance decreases as the dichroic dye concentration increases in both pre and post UV exposure states. A higher

concentration means more dyes in a given area, which in turn absorbs more light. In Figure 25(b), we plot the contrast ratio (CR) versus dichroic dyes concentration. As the dye concentration increases, CR increases. However, the trade-off is compromised transmittance.

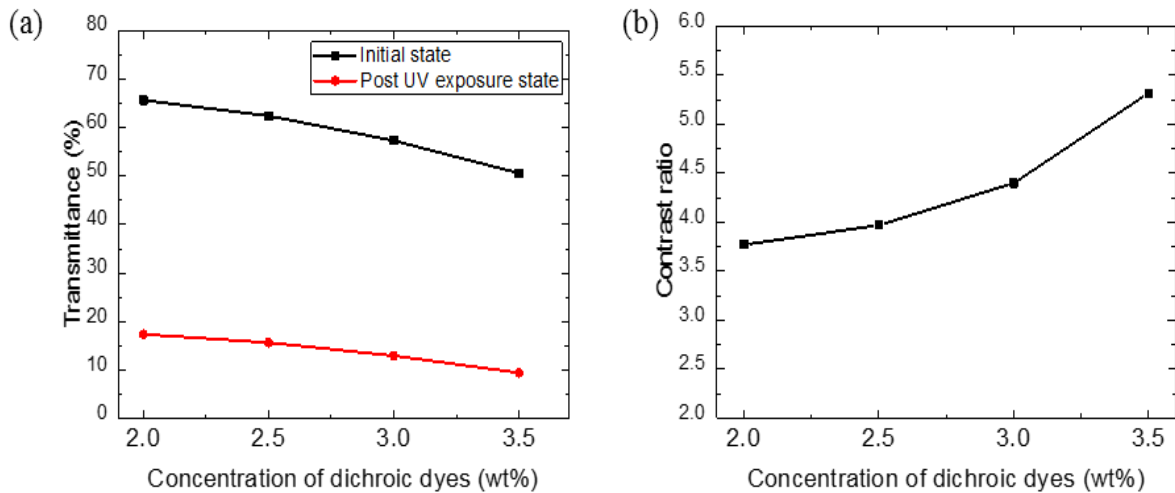


Figure 25 (a) Measured transmittance vs. dyes concentration before and after UV exposure. (b) Contrast ratio vs. dyes concentration.

Finally, we inspected the CLC sample 1(2% dye) under a polarizing optical microscope between crossed polarizers. Figure 26 depicts the microscopic images at pre and post UV exposure state. Before UV exposure (Figure 26(a)), the LC directors and dye molecules are all perpendicular to the substrate surface. As a result, the image appears black. Figure 26(b) shows the post UV exposure state where the LC molecules and dyes are switched to fingerprint state (Figure 19(b)). In this state, helical axis is parallel to the cell surface. The dark lines in Figure 26(b) are the oil streaks where the cholesteric layers are bent [85].

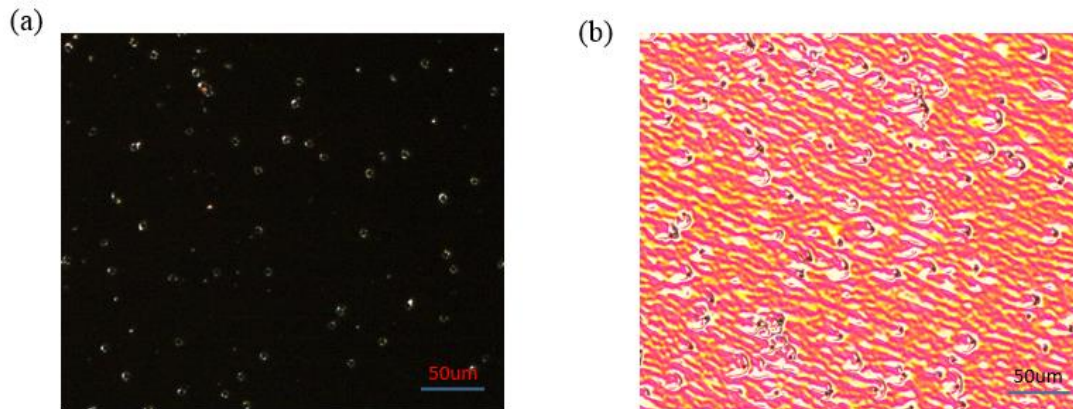


Figure 26 Microscopic image at (a) initial state, and (b) post UV exposure state.

#### 4.4. Summary

We have demonstrated a smart dimmer using a photoresponsive azobenzene and dye-doped cholesteric liquid crystal. Unlike a commercial photochromic transition glass which can only be activated by UV light, our device can be activated by UV and blue light. The dynamic response time is comparable. Potential applications of such a smart dimmer for enhancing the ambient contrast ratio of augmented reality displays and automotive displays are foreseeable.

## CHAPTER 5: DUAL-STIMULI LIQUID CRYSTAL SMART DIMMER

In this chapter, we report a dual-stimuli dye-doped LC smart dimmer with a much faster response time. To achieve dual-stimuli responses, we dope some photo-stable chiral agent, photosensitive azobenzene, and dichroic dye into a nematic LC host with positive dielectric anisotropy ( $\Delta\epsilon > 0$ ). Upon UV light exposure, our device turns from initially vertical alignment (high transmittance state) to twisted fingerprint structure (dark state). The reversal process is accelerated by combining electric field (to unwind the fingerprint to homeotropic alignment) and red light (to transform azobenzene from cis to trans) because the LC host has a positive  $\Delta\epsilon$ . Such an electric-field-assisted reversal time can be reduced from  $\sim 10$  seconds to a few milliseconds, depending on the applied voltage.

### 5.1. Experimental configuration

Our liquid crystal mixture consists of four components: 1-4 wt.% left-handed photo-stable chiral agent (Merck S-811), 0.3-1.3 wt.% right-handed photo-responsive chiral azobenzene compound (PSC-01) [76], [77], 2 wt.% black dichroic dye (Mitsui S428), and an LC host ZLI-2976 ( $\Delta\epsilon = 11$  at  $f = 1$  kHz, clearing temperature  $T_c = 101.7^\circ\text{C}$  and birefringence  $\Delta n = 0.12$  at  $\lambda = 589$  nm). The mixture was stirred on a heating stage for several minutes to dissolve completely. Afterward, the mixture was injected to a  $9\text{-}\mu\text{m}$  homeotropic cell where the LC directors were aligned perpendicular to the glass substrates. Commercial light sources, AMSCOPE UV LED lamp (365nm), blue (450nm) and red light (633nm) sources were used to irradiate the sample. Deuterium halogen light source (DH-2000), He-Ne laser beam

(633nm) and HR4000CG-UV-NIR spectrometer from Ocean Optics were used to measure the spectrum and response time at different state. We used Olympus BX51 polarizing optical microscope to take the images of the sample.

## 5.2. Operation principles

A smart dimmer should be polarization independent because the ambient light is unpolarized. For this purpose, we doped dichroic dyes to a helical LC structure. Dichroic dyes are low molecular weight with elongated dimension. They preferentially absorb the light polarized along the longer axis and transmit the other. However, due to limited dichroic ratio (<15:1), the absorption will not be perfect. When the LC directors and dichroic dyes form cholesteric structure, the absorption is insensitive to polarization. Cholesteric structure are typically prepared by adding a chiral compound to the LC host to induce helical structure. In our device, we mixed a photo-stable chiral agent (S-811) and a photosensitive azobenzene dye (PSC-01) to the dye-doped LC mixture to induce chirality. Helical twist power (HTP) is used to define the chirality, and the net HTP of our mixture depends on the competition between the left-handed chiral agent (S-811, negative HTP) and right-handed azobenzene dyes (PSC-01, positive HTP). However, the HTP of right-handed azobenzene dyes changes upon trans-cis isomerization [86], [87]. Typically, azobenzene dyes stay in rod shape trans-state in the absence of UV-blue light [78], [80]. It has a broad absorption spectrum near UV region and the exposure to UV light changes the molecular conformation. Hence, the trans-azobenzene transforms into the cis-state; the latter has a smaller HTP than the former.

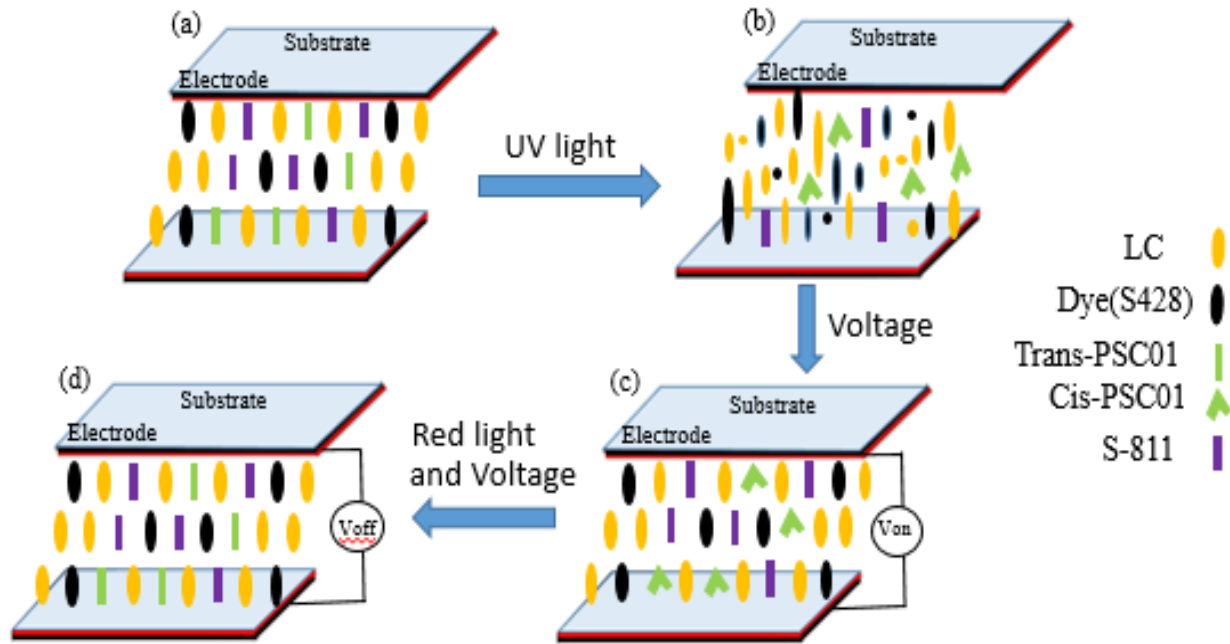


Figure 27 Operation mechanisms of the proposed device: (a) Initial state, (b) after UV exposure, (c) with a voltage, and (d) removing the voltage and red light.

Figure 27 depicts the operation mechanisms of our device. Initially, the concentrations of S-811 and PSC-01 are carefully chosen so that the positive HTP of PSC-01 cancels out the negative HTP of S-811, i.e. the net chirality is too weak to induce cholesteric helical structure. Because the mixture is confined in a cell with sufficiently strong homeotropic anchoring, the LC directors and dichroic dyes will be aligned in vertical direction, as Figure 27(a) shows. In this unwound state, the light absorption is minimum and the device is in the transparent state.

The threshold pitch value to form helical structure is governed by  $P_{th} = 2dK_{22}/K_{33}$ , where  $d$  is the cell gap, and  $K_{22}$  and  $K_{33}$  are the twist and bend elastic constants, respectively

[82]. In an LC cell, when the net pitch value is smaller than the threshold pitch, twisted nematic structure occurs because the chiral torque is strong enough in comparison with the elastic torque. When the LC cell is exposed to UV-blue light, the trans-cis isomerization of azobenzene dye takes place and its positive HTP decreases while the negative HTP of photo-stable chiral agent remains unchanged. As a result, the net absolute HTP value of the mixture increases. When the pitch value is smaller than the threshold pitch, as shown in Figure 27(b), phase transition from homeotropic texture to twisted cholesteric structure occurs. Under such an LC director configuration, the absorption of dichroic dyes is insensitive to the incident light polarization, and the device turns into dark state. A typical contrast ratio of guest-host displays is about 3-5:1. Contrast ratio can be further improved by using a better dye with larger dichroic ratio, or increasing the dye's concentration or LC layer thickness, but the last two approaches would decrease the transmittance. To change from dark to bright state, we can illuminate the device with a red light or apply a voltage. Upon red light exposure, the cis-azobenzene dyes are transformed back to trans-state, and therefore the net HTP decreases. When the net HTP is zero or weaker than the homeotropic anchoring, the pitch value exceeds the threshold value so that the helix is suppressed and the twisted fingerprint-to-homeotropic phase transition takes place. At this state, the device becomes transparent again due to minimum absorption. However, this reversal process takes around 10-20 seconds, depending on the red light intensity.

In order to accelerate the transition from dark to transparent state, we can also apply a voltage. Because our employed nematic host has a positive dielectric anisotropy, the LC directors and dichroic dyes will be unwound from fingerprint to homeotropic state by the

electric field. When a longitudinal electric field is applied at cis-state where the device appears dark, as the electric torque exceeds the chiral torque, the LC directors and dyes will be reoriented back to their initial homeotropic state although the azobenzene molecules remain in cis-state [Figure 27(c)]. Under such condition, as will be shown in next section, the transmittance remains the same as that of Figure 27(a). However, if the voltage is removed, the device will return to dark state quickly [Figure 27(b)]. If we keep irradiating red light to the device for about 10-15 seconds (no matter the voltage is on or off), the cis-azobenzene will be converted back to trans-state and the chiral torque is weaker than the surface anchoring. As a result, the device will stay at transparent state even if we turn-off the voltage. As shown in Figure 27(d), both LC directors and dyes are in vertical alignment and azobenzene is in trans-state, which is the same as Figure 27(a).

### **5.3. Results and discussion**

Figure 28 shows the absorption spectrum of 2% dichroic dye aligned in a direction perpendicular or parallel to the incident polarized light. Red line in Figure 28 shows the absorption of the dye when polarization of the incident light is aligned parallel to the long axis of the dye molecules. Black line in Figure 28 shows the absorption of the dye when polarization of the incident light is perpendicular to the long axis of the dye molecules. Transformation between bright and dark state of our proposed device is based on this absorption properties of dichroic dyes.



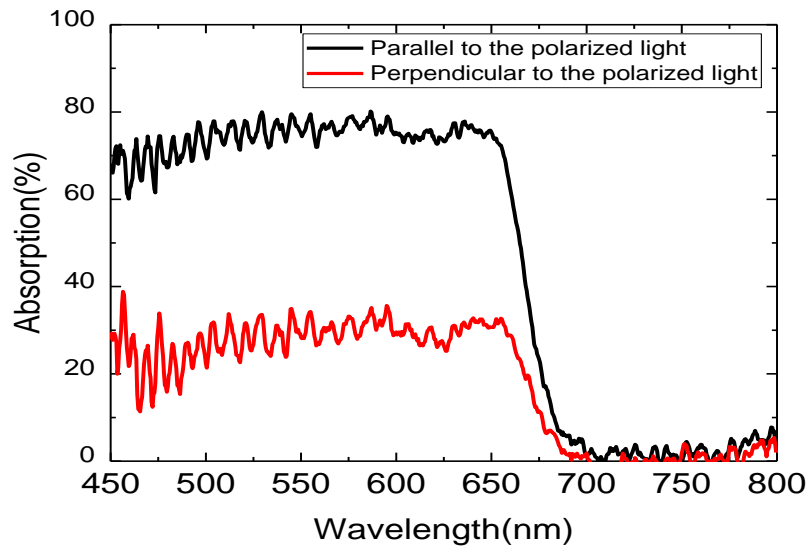


Figure 28 Measured absorption spectrum of 2% dichroic dye in a given LC cell.

We also measured the dichroic ratio of Mitsui dye S428 in the LC host ZLI-2976. To do so, we prepared 3 homogeneous LC cells with 9- $\mu\text{m}$  gap and 1%, 2%, and 4% dye concentrations, and measured their transmittance  $T = \exp(-\alpha d)$ , where  $\alpha d$  represents the absorbance. Figure 29 shows the measured absorbance in two orthogonal polarizations. When the incident polarization is parallel to the long axis of dye molecules, the absorption is high (red line). However, when the polarization of incident light is perpendicular to the long axis of dye molecules, the absorption is decreased (black line). From the slopes of these two straight lines shown in Figure 29, we obtain the dichroic ratio of Mitsui S428 is 11.6 in the ZLI-2976 LC host.

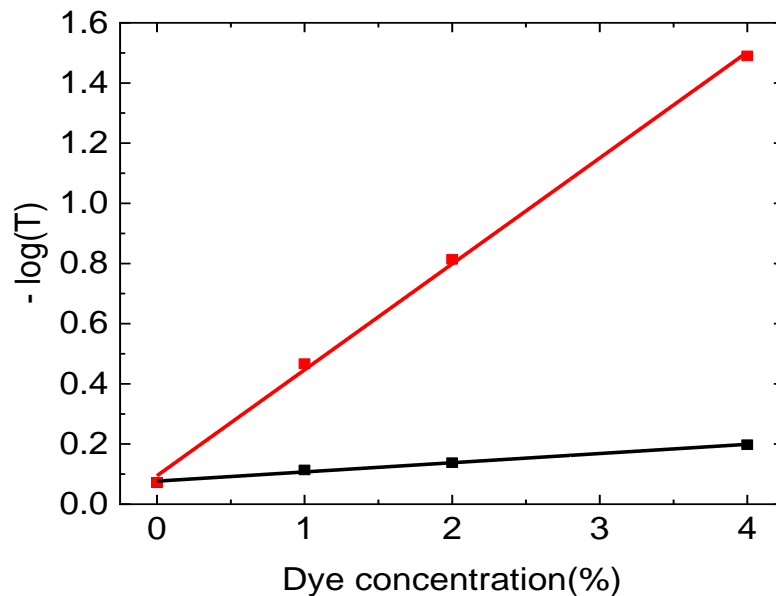


Figure 29 Measured absorption anisotropy of Mitsui S428 dye at  $\lambda=633$  nm. Red and black dots correspond to the polarization parallel and perpendicular to the LC directors. LC host ZLI-2976.

Figure 30 shows the measured transmission spectrum of our guest-host device from 400 nm to 700 nm at the room temperature (22°C). The results shown in Fig. 3 are obtained from the sample containing 4wt% chiral agent and 0.7wt% azobenzene dye. At initial state, the transmittance is relatively high (60-70%) in the visible region due to low absorption loss. Limited dichroic ratio, order parameter, and surface reflection also contribute to the rest of the loss. When the sample is irradiated with a UV light ( $\lambda \approx 365$  nm) at 10 mW/cm<sup>2</sup> intensity, its transmittance decreases in the visible region, as the red line in Fig. 3 shows. For example, at 550 nm, the transmittance drops from  $\sim 70\%$  to  $\sim 23\%$ . After UV exposure, the LC directors and dichroic dyes turn into twisted fingerprint state. In this state, dichroic dyes strongly absorb the incident light and the device turns to dark state including  $\sim 5\%$  scattering. When

the UV light is removed, the device stays at fingerprint state. The twisted fingerprint state is very stable and can last for more than 10 hours.

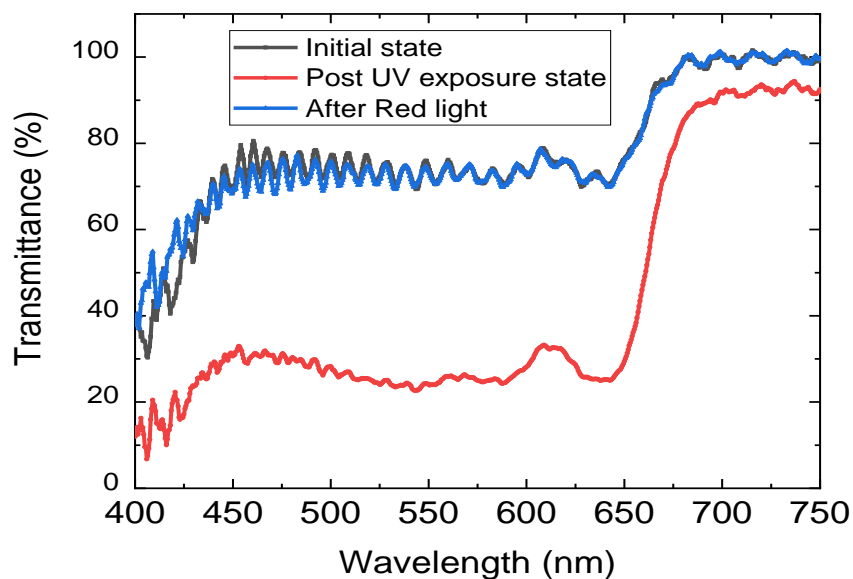


Figure 30 Measured transmission spectra at initial state, post UV exposure, and after red light exposure.

The reversal process from dark to bright state was carried out by exposing the sample with a red light (633nm) at 5.5 mW/cm<sup>2</sup> intensity (blue line in Figure 30). Besides red light, the reversal process can also be carried out by voltage. Figure 31 shows the measured transmittance change after applying different voltages at the post UV exposure state. As the voltage increases, the LC directors and dichroic dyes start to unwind but the transmittance decreases initially due to light scattering. Above 6V, transmittance starts to increase because of the reduced absorption and scattering. At ~10V, the LC directors and dyes are unwound completely and they turn into homeotropic state whereas azobenzene remains in the cis-

state. Therefore, the device returns back to transparent state. Please note the electric field alone cannot transform the cis-azobenzene back to trans-state; additional red (or green) light exposure is required.

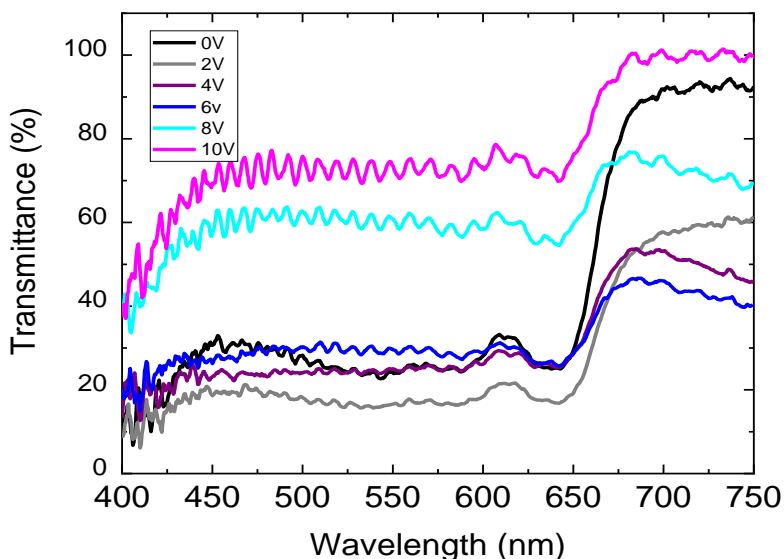


Figure 31 Measured transmission spectra of post UV exposure state under different voltages.

Figure 32 shows the images behind our dimmer at different states. The photos were taken under the lab yellow lighting environment. Figure 32(a) shows the transparent image at initial state where the sample is not exposed to UV light. From this image we can easily recognize the colored word “LCD”. Figure 32(b) shows the image at post UV exposure state. The image becomes dark as transmittance decreases due to trans-cis isomerization. Contrast ratio can be improved by increasing the dichroic dye concentration or using a thicker cell gap, but the trade-off is decreased transmittance. We applied 10V in the center area (with indium tin oxide (ITO) electrodes) at post UV exposure state and the image in this state is shown in Figure 32(c). The LCs and dyes in the electrode area are reversed back to the initial

vertical state due to strong electric field, so that the image “LCD” becomes transparent again. However, the azobenzene remains in the cis-state (Figure 27(c)). To convert the cis back to trans, we exposed the sample with a red light ( $\lambda=633$  nm at intensity= 5.5 mW/cm<sup>2</sup>) for ~20 seconds. This process is independent of whether the voltage is on or off. Figure 32(d) shows the transparent image, which is the same as Figure 32(a).

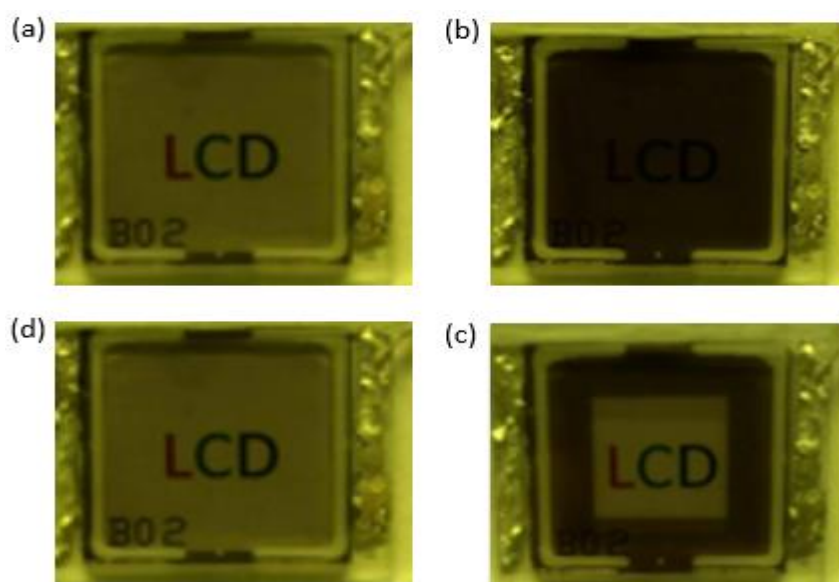


Figure 32 See-through image behind the dimmer: (a) Initial state, (b) Post UV exposure state, (c) After applying 10V at post UV exposure state (the dark area has no electrode), and (d) After red light irradiation for 15 s at post UV exposure state.

We also measured the response time of our device from bright (Figure 32(a)) to dark state (Figure 32(b)) upon UV exposure. Figure 33 shows the measured transmittance (at  $\lambda=633$  nm) versus UV exposure time. The intensity of UV light was measured as 10 mW/cm<sup>2</sup>. From Figure 33, the response time (defined as transmittance changes from 90% to 10%) is 1.3 second. This response time could be further decreased by increasing the UV intensity

[40] or using a faster azobenzene material [84]. It should be mentioned that this device stayed at dark state several hours after the UV light was turned-off.

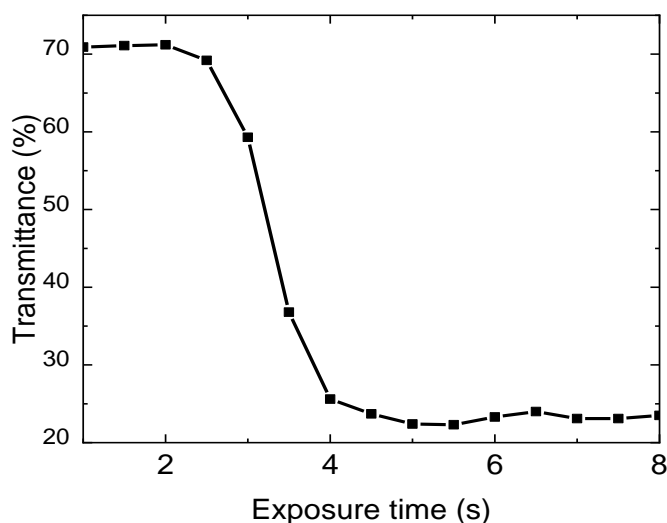


Figure 33 Measured transmittance change at  $\lambda=633$  nm of our device upon UV exposure ( $10$  mW/cm<sup>2</sup>).

At the post-UV exposure state, we applied 10V to the LC sample for 500 ms and recorded the reversal time from dark state to bright state. Results are shown in Figure 34. From Figure 34, the reversal time from dark to bright is about 202 ms. This reversal time is much faster than that of photo-driven device reported earlier [41]. However, when we turned off the voltage the device returns back to dark state within 36.7 ms, as shown in Figure 34. This is because the cis-azobenzene molecules bring the neighboring LCs and dyes back to the twisted fingerprint state, which is a stable state (Figure 32(b)). On the other hand, the voltage-on state (Figure 32(c)) is not a stable state, although its transmittance is the same as that of original state. To work as a dimmer, we can operate the device between these two

states [Figure 32(b) and Figure 32(c), corresponding to Figure 27(b) and Figure 27(c)] because of its fast response time.

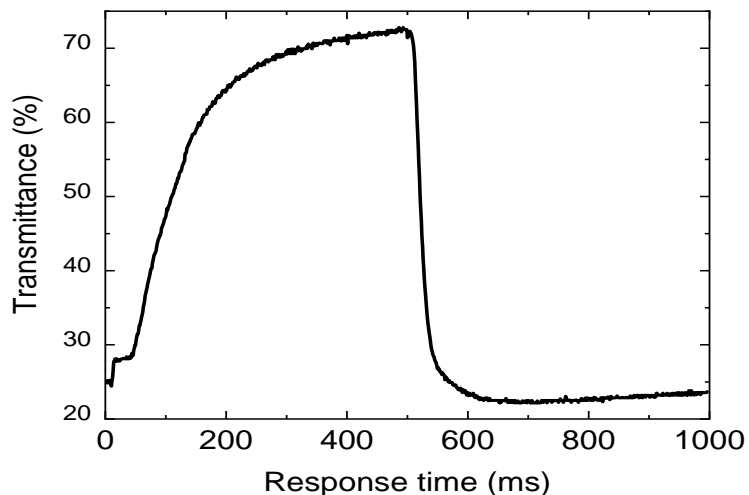


Figure 34 Measured transmittance (at 633 nm) vs. response time at post UV exposure state after applying 10 V for 500 ms.

Reversal time can be shortened by increasing the voltage. If we increase the voltage to 50V, then the reversal time is reduced to  $\sim 8$  ms. Figure 35 shows the measured transmittance vs. response time at post UV exposure state after applying 50v for 100 ms. As shown in Figure 35, transmittance is decreased to  $\sim 8$ ms when it increased to 50v.

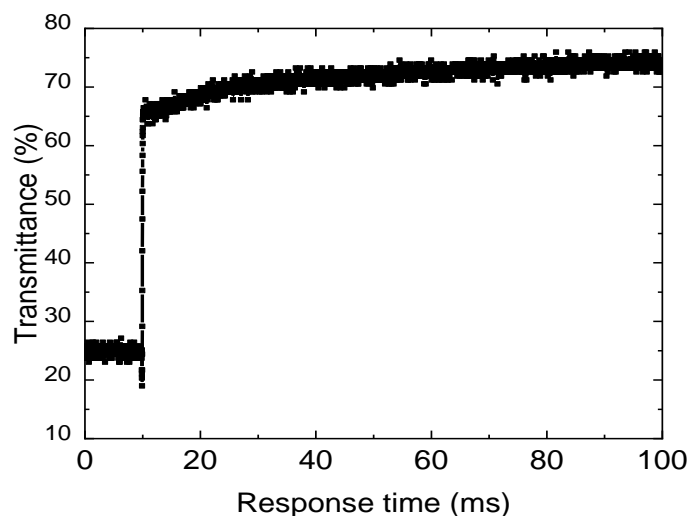


Figure 35 Measured transmittance (at 633 nm) vs. response time at post UV exposure state after applying 50 V for 100 ms.

In order to return to the original stable state, we need to expose the sample with a red light. In experiment, we used a HeNe laser beam with  $\lambda=633$  nm and intensity= 5.5 mW/cm<sup>2</sup>. Figure 36 shows the measured results. Due to red light irradiation, reversal *cis-trans* isomerization takes place and the HTP of azobenzene dye is slowly decreasing. After ~15-20 seconds (Figure 36), the HTP of left-handed S-811 and right-handed PSC-01 cancels out each other and the device stays transparent even if we remove the red light.



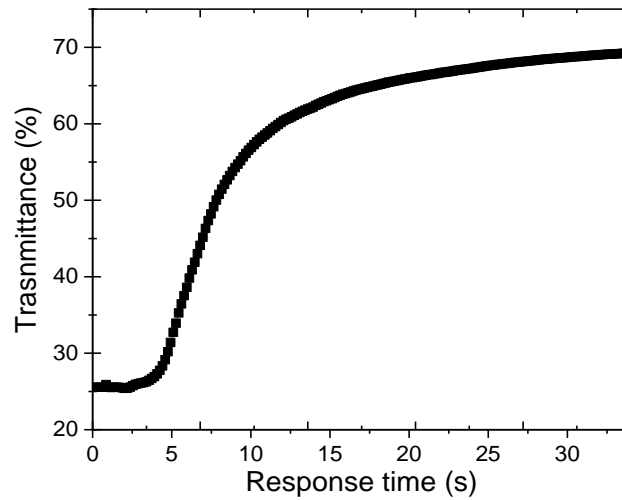


Figure 36 Measured time-dependent transmittance of the LC sample from the post exposure state after HeNe laser beam exposure at intensity= 5.5 mW/cm<sup>2</sup>.

We also applied the the voltage and red light in together. Figure 37 shows the transmittance vs time of our device in post-exposure state when redlight and voltage are applied in together at different time interval.

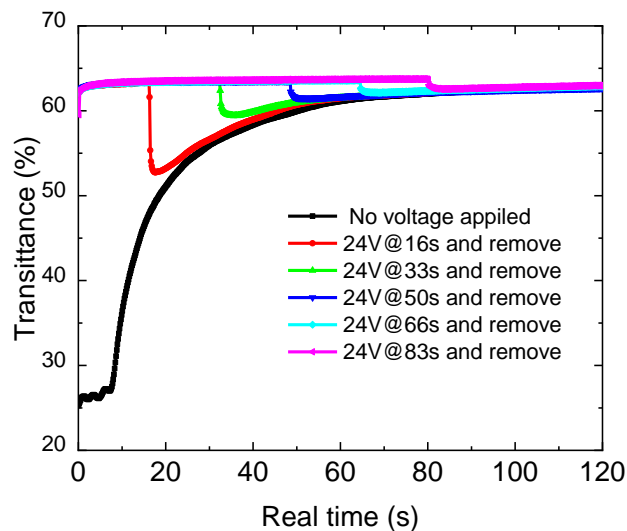


Figure 37 Measured time-dependent transmittance of the LC sample from the post exposure state when red light and voltage are applied together at different time interval.

Some groups are exploring the possibility of electro-isomerization of azobenzene materials. If successful, then we can eliminate the step of red light exposure [88], [89].

Next, we investigate how the concentration of left-handed chiral agent S-811 affects the performance of our device. We prepared four samples by varying the S-811 concentration from 1 wt.% to 5 wt.%, while keeping other material's concentration unchanged (0.7% PSC and 2% S-428) and inspected the samples under a polarizing optical microscope between crossed polarizers. Figure 38(a)-(d) shows the microscopic image at initial state and post UV exposure state for the 1%, 3% and 4% of S-811 samples. As shown in Figure 38(a), at initial state with 1%, 3%, and 4% concentrations the microscope image looks black because the LC directors and dyes are aligned perpendicular to the substrates. However, at the post UV exposure state Figure 38(b)-(d) the fingerprint textures appear. As

the concentration of S-811 increases, the pitch of fingerprint state decreases and well-defined fingerprint texture forms which reduces light scattering.

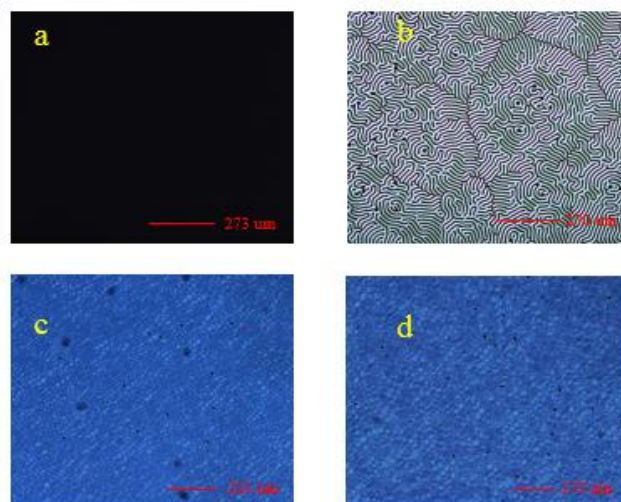


Figure 38 Microscope images of four samples: (a) Initial state (1%-4% S-811), (b) 1% S-811, (c) 3% S-811, and (d) 4% S-811 at post UV exposure state.

Finally, we prepared four samples by varying the concentration of azobenzene from 0.3% to 1.6%, while keeping 4% S-811. Figure 39 shows the microscopic image of these samples which is fingerprint structure.

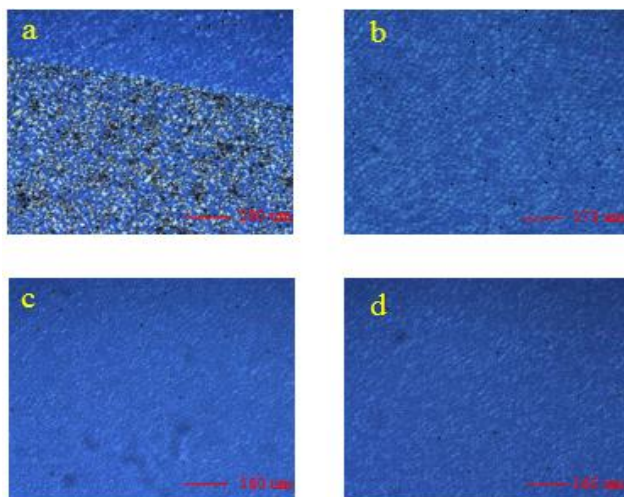


Figure 39 Microscopic images of samples(4% S-811): (a) 0.3%-PSC01 (b) 0.7% PSC01 (c) 1.2% PSC01 (d) 1.6% PSC01 at post exposure state.

Figure 40 shows the measured results of transmittance versus azobenzene concentration in the post UV exposure state and after voltage. From Figure 40, we do not observe any noticeable difference in transmittance in both bright and dark states. It is apparent that at initial state, the HTP of azobenzene within this concentration range still cancels out the HTP of the 4% S-811. However, if azobenzene concentration is lower than 0.3% (with 4% S-811), this device does not work as a dimmer based on our proposed mechanisms.

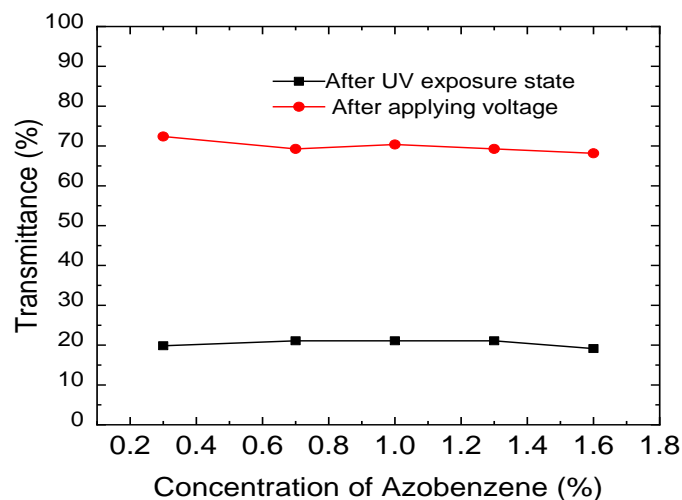


Figure 40 Measured transmittance at different azobenzene concentrations.  $\lambda = 550 \text{ nm}$ .

Lower birefringence liquid crystal helps to suppress the polarization rotation effect of the incident light. Therefore, we also used a lower  $\Delta n$  mixture (ZLI 1800-100,  $\Delta n = 0.07$ , nematic range from  $-20^\circ\text{C}$  to  $61^\circ\text{C}$ ) as host and injected the mixture into a  $9\text{-}\mu\text{m}$  homeotropic cell. Results (Figure 41) are very similar to those of ZLI-2976 (Figure 30) as transmittance of our device mostly depends on the absorption properties of the employed dichroic dye.

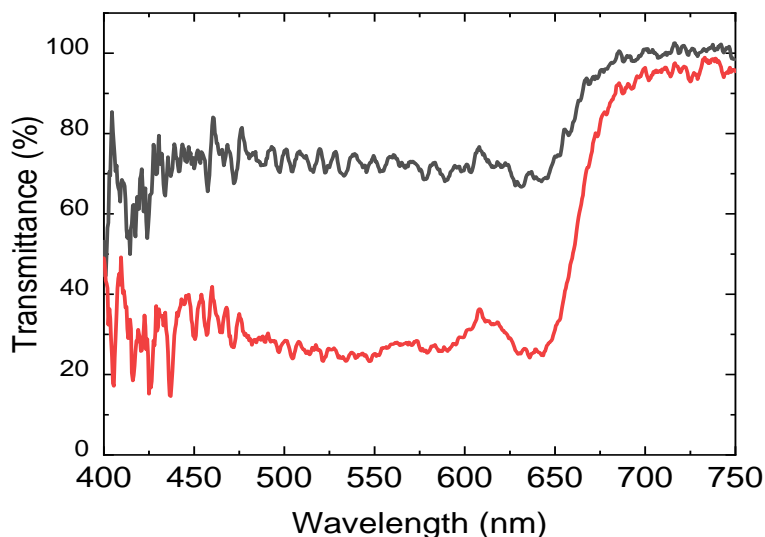


Figure 41 Measured transmission spectra at initial state (black line) and post UV exposure state (red line) using a low birefringence LC host, ZLI 1800-100.

#### 5.4. Summary

We have demonstrated a polarizer-free dual-responsive LC dimmer consisting of chiral compound, dichroic dye, azobenzene, and LC host. Using photo-responsivity of azobenzene dye and absorption properties of dichroic dyes, photo-switching from bright state to dark state is achieved by irradiating UV light. Reversal process from dark to bright state of our device can be carried out by applying a voltage or exposing a red light, or combined together, which offers a significantly faster response time than the previously reported photo-responsive device. Considering its low manufacturing cost and large fabrication tolerance, our photo-responsive device can be used as a light dimmer for augmented reality displays.

## CHAPTER 6: CONCLUSION

High transmittance, fast response, and high ambient contrast ratio are the key parameters for augmented reality (AR) and virtual reality (VR) display systems. In this dissertation, we propose new liquid crystal devices to overcome these challenges.

In chapter 3, we have reported low viscosity liquid crystal material and new electrode configuration for fringe-field switching (FFS) device. We have achieved 67% higher luminance than fast field switching (FFS) mode with virtual wall when compared at 1.5ms motion picture response time (MPRT). Our proposed high transmittance and fast response device can be used in high resolution density and high frame rate displays to resolve the screen door effect, power consumption, and image blurs. Besides, our device also showed high contrast ratio, wide view, indistinguishable color shift, and gamma shift. Therefore, our proposed liquid crystal device can be a potential contender for next generation display technology for augmented reality and virtual reality.

In chapter 4, we have demonstrated a photo-responsive dimmer to solve the ambient contrast ratio of augmented reality displays. Our proposed dimmer consists of right-handed photosensitive chiral azobenzene, left-handed chiral dopant, and dye-doped cholesteric liquid crystal. This device can be activated by low intensity UV and blue light. Reversal process can be carried out by a longer wavelength light (red light) or thermal effect. Main trade-off of this device is slow reversal response time.

In chapter 5, we have demonstrated a fast response dual-stimuli polarizer-free liquid crystal smart dimmer. This device turns from high transmittance homeotropic state to low

transmittance twisted state by applying UV or blue light. Unlike photoresponsive dimmer, reversal process of this device can be accelerated by combining electric field and red light which shows a significant faster response time. Considering the power consumption, low manufacturing cost, and large fabrication tolerance, this dual-stimuli smart dimmer is attractive for augmented reality systems.

In summary, for augmented reality and virtual reality applications, we have focused three crucial display metrics: high luminance, fast motion picture response time, and high ambient contrast ratio. Our diamond shape fringe-field switching device (d-FFS) demonstrated high luminance and fast motion picture response time while fast response dual-stimuli polarizer free smart dimmer can enhance the ambient contrast ratio.



## **APPENDIX: STUDENT'S PUBLICATIONS**

### A. JOURNAL PUBLICATIONS

1. J. R. Talukder, Y. Huang, and S. T. Wu, "High performance LCD for augmented reality and virtual reality displays," *Liq. Cryst.* **46**(6), 920-929 (2019).
2. J. R. Talukder, Y. H. Lee, and S. T. Wu, "Photo-responsive dye-doped liquid crystals for smart windows," *Opt. Express* **27**(4), 4480-4487 (2019).
3. J. R. Talukder, H. Y. Lin, and S. T. Wu, "Photo- and electrical responsive liquid crystal smart dimmer for augmented reality displays," *Opt. Express* **27**(13), (2019).
4. A. Rao, M. Malinowski, A. Honardoost, J. R. Talukder, P. Rabiei, P. J. Delfyett, and S. Fathpour, "Second-Harmonic Generation in Periodically-Poled Thin Film Lithium Niobate Wafer-Bonded on Silicon," *Opt. Express* **24**(26), 29941-29947 (2016).

### B. CONFERENCE PROCEEDINGS

1. J. R. Talukder, Y. Huang, and S. T. Wu, "High transmittance and fast response FFS LCD for AR and VR displays," *SID Symp. Digest* **50** (1), 929-932 (2019, San Jose, CA).
2. J. R. Talukder, S. Utsunomiya, N. Namekata, S. Inoue, K. Takata, K. Wen, K. Yan, Y. Yamamoto, "Polarization switching of injection-locked semiconductor laser, VCSEL," *The Physical Society of Japan*, **67**(2), 133 (2012).
3. H. Chen, Y. Huang, F. Gou, J. R. Talukder, M. C. Li, S. L. Lee, S. T. Wu, "New nematic LCD with submillisecond response time," *SID Symp. Digest* **49**(1), 1691-1694 (2018, Los Angeles, CA).
4. A. Rao, M. Malinowski, A. Honardoost, M. J. R. Talukder, P. Rabiei, P. Delfyett, and S. Fathpour, "Second-Harmonic Generation in Periodically-Poled Thin Film Lithium

Niobate on Silicon,” in *Frontiers in Optics 2016*, OSA Technical Digest (online), paper FTh5G.7 (2016).

## REFERENCES

- [1] J. P. Rolland and H. Fuchs, "Optical versus video see-through head-mounted displays in medical visualization," *Presence-Teleop. Virt.* **9**(12), 287-309 (2000).
- [2] J. Wang, H. Suenaga, K. Hoshi, L. Yang, E. Kobayashi, I. Sakuma, and H. Liao, "Augmented reality navigation with automatic marker-free image registration using 3-D image overlay for dental surgery," *IEEE Trans. Biomed. Eng.* **61**(4), 1295-1304 (2014).
- [3] T. Sielhorst, M. Feuerstein, and N. Navab, "Advanced medical displays: a literature review of augmented reality," *J. Display Technol.* **4**(4), 451-467 (2008).
- [4] X. Hu and H. Hua, "High-resolution optical see-through multi-focal-plane head-mounted display using freeform optics," *Opt. Express* **22**(11), 13896-13903 (2014).
- [5] P. E. Kourouthanassis, C. Boletis, and G. Lekakos, "Demystifying the design of mobile augmented reality applications," *Multimed Tools Appl.* **74**(3), 1045-1066 (2015).
- [6] X. Wang and P. S. Dunston, "Comparative effectiveness of mixed reality-based virtual environments in collaborative design," *IEEE Trans. Syst., Man, Cybern. Syst., Part C (Applications and Reviews)*, **41**(3), 284-296 (2011).
- [7] H. Regenbrecht, G. Baratoff, and W. Wilke, "Augmented reality projects in the automotive and aerospace industries," *IEEE Comput. Graphics Appl.* **25**(6), 48-56 (2005).
- [8] M. Schadt, "Milestone in the history of field-effect liquid crystal displays and materials," *Jpn. J. Appl. Phys.* **48**, 03B001 (2009).
- [9] T. Tsujimura, *OLED Display Fundamentals and Applications*, 2<sup>nd</sup> Ed. (Wiley, 2017).

- [10] H. Hua, "Enabling focus cues in head-mounted display," *Proc. IEEE*, **105**(5), 805-824 (2017).
- [11] H. Chen, F. Gou, and S. T. Wu, "A submillisecond-response nematic liquid crystal for augmented reality displays," *Opt. Mater. Express* **7**(1), 195-201 (2017).
- [12] H. Chen, J. H. Lee, B.Y. Lin, S. Chen, and S.T. Wu, "Liquid crystal display and organic light-emitting diode display: Present status and future perspectives," *Light: Science & Applications* **7**, 17168 (2018).
- [13] Y. Igarashi, T. Yamamoto, Y. Tanaka, J. Someya, Y. Nakakura, M. Yamakawa, S. Hasegawa, Y. Nishida, and T. Kurita, "Summary of moving picture response time (MPRT) and futures," *SID Int. Symp. Digest Tech. Papers* **35**(1), 1262–1265 (2004).
- [14] F. Peng, H. Chen, F. Gou, Y. H. Lee, M. Wand, M. C. Li, S. L. Lee, and S. T. Wu, "Analytical equation for the motion picture response time of display devices," *J. Appl. Phys.* **121**(2), 023108 (2017).
- [15] C. Murawski K. Leo, M.C. Gather, "Efficiency roll-off in organic light-emitting diodes," *Adv. Mater.* **25**, 6801-6827 (2013).
- [16] C. Féry, B. Racine, D. Vaufrey, H. Doyeux, and S. Cinà, "Physical mechanism responsible for the stretched exponential decay behavior of aging organic light-emitting diodes," *Appl. Phys. Lett* **87**, 213502 (2005).
- [17] S. H. Lee, S. L. Lee, and H. Y. Kim, "Electro-optic characteristics and switching principle of a nematic liquid crystal cell controlled by fringe-field switching," *Appl. Phys. Lett.* **73**(20), 2881–2883 (1998).

- [18] Z. Deng, B. Zheng, J. Zheng, L. Wu, W. Yang, Z. Lin, P. Shen, and J. Li, "High dynamic range incell LCD with excellent performance," *SID Symp. Dig. Tech. Papers* **49(1)**, 996-998 (2018).
- [19] G. Tan, Y. Huang, M.C. Chen, S. L. Lee, and S. T. Wu, "High dynamic range liquid crystal displays with a mini-LED backlight," *Opt. Express* **26(13)**, 16572-16584 (2018).
- [20] M. Jiao, Z. Ge, S. T. Wu, and W. K. Choi, "Submillisecond response nematic liquid crystal modulators using dual fringe-field switching in a vertically aligned cell," *Appl. Phys. Lett.* **92**, 111101 (2008).
- [21] T. Matsushima, K. Okazaki, Y. Yang, and K. Takizawa, "New fast response time in-plane switching liquid crystal mode," *SID Int. Symp. Digest Tech. Papers* **46**, 648 (2015).
- [22] T.-H. Choi, S.-W. Oh, Y.-J. Park, Y. Choi, and T.-H. Yoon, "Fast fringe-field switching of a liquid crystal cell by two-dimensional confinement with virtual walls," *Sci. Rep.* **6**, 27936 (2016).
- [23] T. Katayama, S. Higashida, A. Kanashima, K. Hanaoka, H. Yoshida, S. Shimada, "Development of in-plane super-fast response (ip-SFR) LCD for VR-HMD," *SID Int. Symp. Digest Tech. Papers* **49(1)**, 671-673 (2018).
- [24] R. Zhu, H. Chen, T. Kosa, P. Coutino, G. Tan, and S. T. Wu, "High-ambient-contrast augmented reality with a tunable transmittance liquid crystal film and a functional reflective polarizer," *J. Soc. Inf. Disp.* **24(4)**, 229-233 (2016).
- [25] S. Lee, X. Hu, and H. Hua, "Effects of optical combiner and IPD change for convergence on near-field depth perception in an optical see-through HMD," *IEEE Trans. Vis. Comput. Graphics.* **22(5)**, 1540-1554 (2016).

- [26] R. Zhu, G. Tan, J. Yuan, and S. T. Wu. "Functional reflective polarizer for augmented reality and color vision deficiency." *Opt. Express* **24**(5), 5431-5441 (2016).
- [27] R. Chen, Y. H. Lee, T. Zhan, K. Yin, Z. An, and S. T. Wu, "Multi-stimuli-responsive self-organized liquid crystal Bragg gratings," *Adv. Opt. Mater.* **7**, 1900101 (2019).
- [28] E. L. Runnerstrom, A. Llordés, S. D. Lounis, and D. J. Milliron, "Nanostructured electrochromic smart windows: traditional materials and NIR-selective plasmonic nanocrystals," *Chem. Commun.* **50**(73), 10555-10572 (2014).
- [29] A. Tsuboi, K. Nakamura, and N. Kobayashi, "Multicolor electrochromism showing three primary color states (cyan–magenta–yellow) based on size-and shape-controlled silver nanoparticles," *Chem. Mater.* **26**(22), 6477-6485 (2014).
- [30] Y.-M. Zhang, X. Wang, W. Zhang, W. Li, X. Fang, B. Yang, M. Li, and S. X.-A. Zhang, "A single-molecule multicolor electrochromic device generated through medium engineering." *Light: Sci. & Appl.* **4**(2), e249 (2015).
- [31] J. A. Kerszulis, C. M. Amb, A. L. Dyer, J. R. Reynolds, "Follow the yellow brick road: structural optimization of vibrant yellow-to-transmissive electrochromic conjugated polymers," *Macromolecules* **47**(16), 5462-5469 (2014).
- [32] V. Vasilyeva, P. M. Beaujuge, S. Wang, J. E. Babiartz, V. W. Ballarotto, and J. R. Reynolds, "Material strategies for black-to-transmissive window-type polymer electrochromic devices," *ACS Appl. Mater. Interfaces*, **3**(4), 1022-1032 (2011).
- [33] W. Wen, C. Weisbuch, D. Phuong, G. Lu, W. Ge, C. T. Chan, and P. Sheng, "Neutral nanoparticle-based display," *Nanotechnology* **16**(4), 598 (2005).

- [34] A. Ghosh, B. Norton, and A. Duffy, "Measured overall heat transfer coefficient of a suspended particle device switchable glazing," *Appl. Energy* **159**, 362-369(2015).
- [35] J. Heo, J.-W. Huh, and T.-H. Yoon "Fast-switching initially-transparent liquid crystal light shutter with crossed patterned electrodes," *AIP Advances* **5**(4), 047118 (2015).
- [36] Y.-H. Lin, J.-M. Yang, Y.-R. Lin, S.-C. Jeng, and C.-C. Liao, "A polarizer-free flexible and reflective electro-optical switch using dye-doped liquid crystal gels," *Opt. Express* **16**(3), 1777-1785 (2008).
- [37] G. H. Lee, K. Y. Hwang, J. E. Jang, Y. W. Jin, S. Y. Lee, and J. E. Jung, "Characteristics of color optical shutter with dye-doped polymer network liquid crystal," *Opt. Lett.* **36**(5), 754-756 (2011).
- [38] C.-T. Wang and T.-H. Lin, "Bistable reflective polarizer-free optical switch based on dye-doped cholesteric liquid crystal [Invited]," *Opt. Mater. Express* **1**(8), 1457-1462 (2011).
- [39] Y. H. Lin, H. W. Ren, and S. T. Wu, "High contrast polymer-dispersed liquid crystal in a 90° twisted cell," *Appl. Phys. Lett.* **84**(20), 4083-4085 (2004).
- [40] J. R. Talukder, Y. H. Lee, and S.-T. Wu, "Photo-responsive dye-doped liquid crystals for smart windows," *Opt. Express* **27**(4), 4480-4487 (2019).
- [41] D. K. Yang, J. W. Doane, Z. Yaniv, and J. Glasser, "Cholesteric reflective display: drive scheme and contrast," *Appl. Phys. Lett.* **64**(15), 1905–1907 (1994).
- [42] A. Bobrovsky, N. Boiko, V. Shibaev, and J. Wendorff, "Photoinduced textural and optical changes in a cholesteric copolymer with azobenzene-containing side groups," *Liq. Cryst.* **31**(3), 351-359 (2004).



- [43] G. H. Heilmeyer and L. A. Zanoni, "Guest-host interactions in nematic liquid crystals," *Appl. Phys. Lett.* **13**(3), 91–92 (1968).
- [44] D. L. White and G. N. Taylor, "New absorptive mode reflective liquid-crystal display device," *J. Appl. Phys.* **45**(11), 4718–4723 (1974).
- [45] A. V. Ivashchenko, *Dichroic liquid-crystal displays* (CRC Press, 1994).
- [46] D. K. Yang, "Review of operating principle and performance of polarizer-free reflective liquid-crystal displays," *J. Soc. Inf. Disp.* **16**(1), 117-124 (2008).
- [47] C. T. Wang, Y. C. Wu, and T. H. Lin, "Photo-controllable tristable optical switch based on dye-doped liquid crystal," *Dyes and Pigments* **103**, 21-24 (2014).
- [48] S. W. Oh, J. M. Baek, J. Heo, and T. H. Yoon, "Dye-doped cholesteric liquid crystal light shutter with a polymer-dispersed liquid crystal film," *Dyes and Pigments* **134**, 34-40 (2016).
- [49] P. G. de Gennes and J. Prost, *The Physics of Liquid Crystals* (Oxford University Press, 1993).
- [50] P. Oswald and P. Pieranski, *Nematic and Cholesteric Liquid Crystals: Concept and Physical Properties Illustrated by Experiments* (CRC Press, 2005).
- [51] S. Kurihara, S. Nomiya, and T. Nonaka, "Photochemical control of the macrostructure of cholesteric liquid crystals by means of photoisomerization of chiral azobenzene molecules," *Chem. Mater.* **13**(6), 1992–1997 (2001).
- [52] J. Bin and W. S. Oates, "A unified material description for light induced deformation in azobenzene polymers," *Sci. Rept.* **5**, 14654 (2015).

- [53] Y. Zhao and T. Ikeda, *Smart Light-Responsive Materials* (John Wiley and Sons, Hoboken, NJ, 2009).
- [54] Oh-e, Masahito, and K. Kondo, "Electro-optical characteristics and switching behavior of the in-plane switching mode," *Applied physics letters* **67** (26), 3895-3897(1995).
- [55] S. H. Lee, S. L. Lee, and H. Y. Kim, "Electro-optic characteristics and switching principle of a nematic liquid crystal cell controlled by fringe-field switching," *Applied physics letters* **73**(20), 2881-2883(1998).
- [56] T.-H. Choi, J.-H. Woo, Y. Choi, and T.-H. Yoon, "Interdigitated pixel electrodes with alternating tilts for fast fringe-field switching of liquid crystals," *Opt. Express* **24**(24), 27569-27576 (2016).
- [57] Y. Chen, F. Peng, T. Yamaguchi, X. Song, S. T. Wu, "High performance negative dielectric anisotropy liquid crystals for display applications," *Crystals*. **3**(3):483-503 (2013).
- [58] R. Hatsumi, S. Fukai, Y. Kubota, A. Yamashita, M. Jikumaru, H. Baba, K. Moriya, D. Kubota, K. Kusunoki, Y. Hirakata, and J. Koyama, "FFS-mode OS-LCD for reducing eye strain. *Journal of the Society for Information Display*, **21**(10), 442-450 (2013).
- [59] J.W. Ryu, J.Y. Lee, H.Y. Kim, J.W. Park, G.D. Lee, S.H. Lee, "Effect of magnitude of dielectric anisotropy of a liquid crystal on light efficiency in the fringe-field switching nematic liquid crystal cell," *Liq. Cryst.* **35**(4), 407-411(2008).
- [60] S.W. Kang, I.W. Jang, D.H. Kim, Y.J. Lim, S.H. Lee, "Enhancing transmittance of fringe-field switching liquid crystal device by controlling perpendicular component of dielectric constant of liquid crystal," *Jpn. J. Appl. Phys.* **53**(1), 010304 (2014).

- [61] H. Takatsu, "Advanced liquid crystal materials for active matrix displays," Conf. Proc. Advanced Display Materials and Devices, p.43 (Sendai, Japan, 2014).
- [62] I. Haller, "Thermodynamic and static properties of liquid crystals," Prog. Solid State Chem. **10**(2), 103–118 (1975).
- [63] S. T. Wu, "Birefringence dispersions of liquid crystals," Phys. Rev. A. **33**(2), 1270–1274 (1986).
- [64] S. T. Wu and C. S. Wu, "Rotational viscosity of nematic liquid crystals A critical examination of existing models," Liq. Cryst. **8**(2), 171–182 (1990).
- [65] D. Xu, F. Peng, G. Tan, J. He, and S.T. Wu, "A semi-empirical equation for the response time of in-plane switching liquid crystal and measurement of twist elastic constant," J. Appl. Phys. **117**, 203103 (2015).
- [66] H. Chen, Y. F. Lan, C. Y. Tsai, and S. T. Wu, "Low-voltage blue-phase liquid crystal display with diamond-shape electrodes," Liq. Cryst. **44**(7), 1124-1130 (2017).
- [67] A. Lien, "Extended Jones matrix representation for the twisted nematic liquid crystal display at oblique incidence," Appl. Phys. Lett. **57**(26), 2767–2769 (1990).
- [68] Z. Ge, S.T. Wu, S.S. Kim, J.W. Park, S.H. Lee, "Thin cell fringing-field-switching liquid crystal display with a chiral dopant," Appl. Phys. **92**, 181109 (2008).
- [69] H. Chen, F. Peng, Z. Luo, D. Xu, S.T. Wu, "High performance liquid crystal displays with a low dielectric constant material," Opt. Mater. Express. **4**(11), 2262–2273 (2014).

- [70] H. Ito, M. Ogawa, and S. Sunaga, "Evaluation of an organic light-emitting diode display for precise visual stimulation," *J. Vis.* **13**(7), 6 (2013).
- [71] F. Gou, H. Chen, M. Li, S. Lee, and S. T. Wu, "Motion-blur-free LCD for high resolution virtual reality displays," *J. Soc. Inf. Disp.* **26**(4), 223-228 (2018).
- [72] S. B. Park, J. K. Song, Y. Um, and K. H. Kim, "Pixel-division technology for high-quality vertical-alignment LCDs," *IEEE Electron Device Lett.* **31**(9), 987-989 (2010).
- [73] S. S. Kim, B. H. Berkeley, K. H. Kim, and J. K. Song, "New technologies for advanced LCD-TV performance," *J. Soc. Inf. Disp.* **12**(4), 353-359 (2004).
- [74] Z. Luo, D. Xu, S.T. Wu, "Emerging quantum-dots-enhanced LCDs," *Journal of display technology* **10**(7), 526-539 (2014).
- [75] H. Chen, J. He, and S. T. Wu, "Recent advances in quantum-dot-enhanced liquid crystal displays," *IEEE. J. Sel. Topics in Quantum Electronics*, **23**(5), 1900611 (2017).
- [76] Y. H. Lee, L. Wang, H. Yang, and S. T. Wu, "Photo-induced handedness inversion with opposite-handed cholesteric liquid crystal," *Opt. Express* **23**(17), 22658-22666 (2015).
- [77] Q. Li, L. Green, N. Venkataraman, I. Shiyankovskaya, A. Khan, A. Urbas, and J. W. Doane, "Reversible photoswitchable axially chiral dopants with high helical twisting power," *J. Am. Chem. Soc.* **129**(43), 12908- 12909 (2007).
- [78] S. Kundu and S.-W. Kang, "Photo-stimulated phase and anchoring transitions of chiral azo-dye doped nematic liquid crystals," *Opt. Express* **21**(25), 31324-31329 (2013).

- [79] M. Mathews and N. Tamaoki, "Reversibly tunable helicity induction and inversion in liquid crystal self-assembly by a planar chiroptic trigger molecule," *Chem. Commun. (Camb.)* **24**(24), 3609–3611 (2009).
- [80] M. Mathews, R. S. Zola, S. Hurley, D.-K. Yang, T. J. White, T. J. Bunning, and Q. Li, "Light-driven reversible handedness inversion in self-organized helical superstructures," *J. Am. Chem. Soc.* **132**(51), 18361–18366 (2010).
- [81] I. Dierking, F. Gießelmann, P. Zugenmaier, W. Kuczynskit, S. T. Lagerwall, and B. Stebler, "Investigations of the structure of a cholesteric phase with a temperature induced helix inversion and of the succeeding Sc\* phase in thin liquid crystal cells," *Liq. Cryst.* **13**(1), 45–55 (1992).
- [82] B. Y. Zeldovich and N. V. Tabiryan, "Equilibrium structure of a cholesteric with homeotropic orientation on the walls," *Sov. Phys. JETP* **56**, 563–566 (1982).
- [83] G. Wirnsberger, B. J. Scott, B. F. Chmelka, and G. D. Stucky. "Fast response photochromic mesostructures." *Adv. Mater.* **12**(19), 1450-1454 (2000).
- [84] U. Hrozhyk, S. Serak, N. Tabiryan, D. Steeves, L. Hoke, and B. Kimball, "Azobenzene liquid crystals for fast reversible optical switching and enhanced sensitivity for visible wavelengths", *Liquid Crystals XIII*, ed. by I.-C. Khoo, *Proc. SPIE*, **7414**, 74140L (2009).
- [85] G. Liao, S. Stojadinovic, G. Pelzl, W. Weissflog, S. Sprunt, and A. Jakli, "Optically isotropic liquid-crystal phase of bent-core molecules with polar nanostructure", *Phys. Rev. E.* **72**(2), 021710 (2005).

- [86] S. Kurihara, S. Nomiya, and T. Nonaka, "Photochemical control of the macrostructure of cholesteric liquid crystals by means of photoisomerization of chiral azobenzene molecules," *Chem. Mater.* **13**(6), 1992–1997 (2001).
- [87] J. Bin and W. S. Oates, "A unified material description for light induced deformation in azobenzene polymers," *Sci. Rept.* **5**, 14654 (2015).
- [88] Y.-C. Liu, K. -T. Cheng, H. -F. Chen, and A. Y.-G. Fuh, "Photo- and electro-isomerization of azobenzenes based on polymer-dispersed liquid crystals doped with azobenzenes and their applications," *Opt. Express* **22**, 4404-4411 (2014).
- [89] Z. F. Liu, K. Hashimoto, and A. Fujishima, "Photoelectrochemical information storage using an azobenzene derivative," *Nature* **347**(6294), 658–660 (1990).